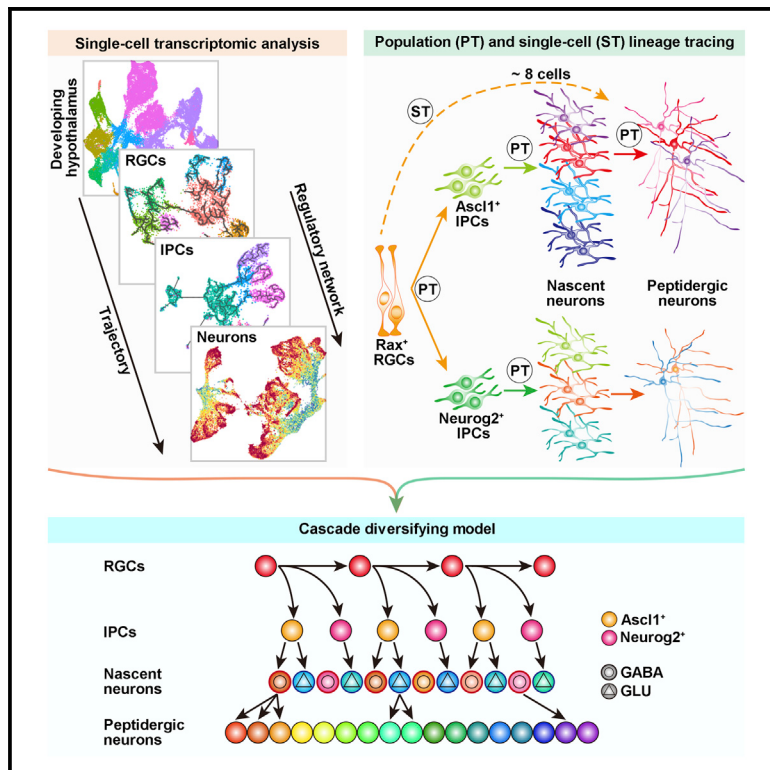


Cascade diversification directs generation of neuronal diversity in the hypothalamus

Graphical abstract



Authors

Yu-Hong Zhang, Mingrui Xu,
Xiang Shi, ..., Miao He, Mingze Yao,
Qing-Feng Wu

Correspondence

wu_qingfeng@genetics.ac.cn

In brief

Zhang et al. combine single-cell transcriptomics with lineage tracing to map the developmental trajectory of the mouse hypothalamus. They find that multiple cell types along the hypothalamic lineage hierarchy enable neuronal multifurcation, revealing a cascade diversification strategy for generating extreme neuronal diversity.

Highlights

- Embryonic radial glial cells (RGCs) are a reservoir for tanyocyte generation
- RGCs and intermediate progenitors undergo cascading fate diversification
- Maturing post-mitotic neurons diversify into multiple peptidergic subtypes
- Single RGCs generate multiple neuronal subtypes



Resource

Cascade diversification directs generation of neuronal diversity in the hypothalamus

Yu-Hong Zhang,^{1,2,7} Mingrui Xu,^{1,2,7} Xiang Shi,^{1,2,7} Xue-Lian Sun,^{1,2,7} Wenhui Mu,^{1,7} Haoda Wu,^{1,2} Jingjing Wang,¹ Si Li,^{1,2} Pengfei Su,³ Ling Gong,⁴ Miao He,⁴ Mingze Yao,³ and Qing-Feng Wu^{1,2,5,6,8,*}

¹State Key Laboratory of Molecular Development Biology, Institute of Genetics and Developmental Biology, Chinese Academy of Sciences, Beijing 100101, China

²University of Chinese Academy of Sciences, Beijing 100101, China

³Institutes of Biomedical Sciences, Shanxi University, Taiyuan 030006, China

⁴Institutes of Brain Science, State Key Laboratory of Medical Neurobiology, Fudan University, Shanghai 200032, China

⁵CAS Center for Excellence in Brain Science and Intelligence Technology, Shanghai 200031, China

⁶Chinese Institute for Brain Research, Beijing 102206, China

⁷These authors contributed equally

⁸Lead contact

*Correspondence: wu_qingfeng@genetics.ac.cn

<https://doi.org/10.1016/j.stem.2021.03.020>

SUMMARY

The hypothalamus contains an astounding heterogeneity of neurons that regulate endocrine, autonomic, and behavioral functions. However, its molecular developmental trajectory and origin of neuronal diversity remain unclear. Here, we profile the transcriptome of 43,261 cells derived from *Rax*⁺ hypothalamic neuroepithelium to map the developmental landscape of the mouse hypothalamus and trajectory of radial glial cells (RGCs), intermediate progenitor cells (IPCs), nascent neurons, and peptidergic neurons. We show that RGCs adopt a conserved strategy for multipotential differentiation but generate *Ascl1*⁺ and *Neurog2*⁺ IPCs. *Ascl1*⁺ IPCs differ from their telencephalic counterpart by displaying fate bifurcation, and postmitotic nascent neurons resolve into multiple peptidergic neuronal subtypes. Clonal analysis further demonstrates that single RGCs can produce multiple neuronal subtypes. Our study reveals that multiple cell types along the lineage hierarchy contribute to fate diversification of hypothalamic neurons in a stepwise fashion, suggesting a cascade diversification model that deconstructs the origin of neuronal diversity.

INTRODUCTION

A mechanistic understanding of brain development requires a systematic survey of neural progenitor cell types, their lineage specification, and developmental maturation of postmitotic neurons. Cumulative evidence based on single-cell transcriptomic analysis have revealed the transcriptional heterogeneity of cortical neural progenitors, their temporal patterning, and the differentiation trajectories of excitatory neurons and inhibitory interneurons in the developing mammalian neocortex (Johnson et al., 2015; Loo et al., 2019; Mayer et al., 2018; Mi et al., 2018; Nowakowski et al., 2017; Zhong et al., 2018). However, the developmental hierarchy of the hypothalamus, representing a conserved but extremely diverse and complex brain structure, remains poorly understood.

The hypothalamus maintains systemic homeostasis of animals by regulating endocrine, autonomic, and behavioral functions ranging from hunger, sleep, thirst, circadian rhythm, and body temperature to mood regulation, sex drive, and hormonal release (Puelles et al., 2012; Sternson, 2013). The functional complexity of the hypothalamus relies on the extreme neuronal

diversity generated during brain development. Hypothalamic neurons are comprised of magnocellular endocrine neurons (OXT [oxytocin], AVP [arginine vasopressin], etc.), parvocellular secretory neurons (TRH [thyrotropin-releasing hormone], CRH [corticotropin-releasing hormone], etc.), large peptidergic projection neurons (HCRT [hypocretin], MCH [melanin-concentrating hormone], etc.), parvocellular peptidergic neurons (POMC [proopiomelanocortin], AgRP [agouti-related protein], etc.), and other inhibitory or excitatory local-circuit neurons (Romanov et al., 2019). Various neuropeptides have long served as a basis for defining neuronal subtypes and understanding hypothalamic functionality. In contrast to numerous studies revealing the circuit and function of diverse hypothalamic neurons, little is known about how neuronal subtype-specific heterogeneity emerges from common radial glial cells (RGCs), acting as embryonic neural stem cells (NSCs) during development. Two models have been proposed for the origin and process of generating neuronal diversity in the mammalian brain. One model proposes that cortical RGCs sequentially produce fate-predetermined intermediate progenitor cells (IPCs) differentiating into deep-layer and upper-layer excitatory neurons (Kohwi and Doe, 2013).



Recent single-cell analyses further support the theory that the diversity of cortical inhibitory interneurons is already predetermined at the level of progenitors or shortly after becoming postmitotic (Mayer et al., 2018; Mi et al., 2018). Notably, the origins of excitatory glutamatergic and inhibitory GABAergic neurons as well as their immediate progenitors are spatially segregated and diverse in the neocortex (Marín and Müller, 2014). The second model postulates that retinal progenitor cells stochastically adopt diverse cell fates during differentiation (Gomes et al., 2011; He et al., 2012). Given the intermingling of molecularly diverse neurons and their critical roles in maintaining homeostatic control, it is fundamentally important to investigate the developmental diversification and trajectories of hypothalamic neurons.

Here we sorted hypothalamic cells arising from the Pax6 lineage for single-cell RNA sequencing and delineated the developmental trajectory of RGCs, IPCs, nascent neurons, and peptidergic neurons within the neural lineage hierarchy. In contrast to the predetermined fate model in the cortex and the stochastic model in the retina, our transcriptomics analysis, in combination with lineage tracing data, supports a cascade diversification model where RGCs, IPCs, and nascent neurons prompt diversification of hypothalamic neuronal fate in a stepwise manner, uncovering an effective strategy for neural progenitors to generate extreme neuronal diversity. We also identified the embryonic origin of postnatal tanyocytes and the regulons specifying neuronal subtypes, which further provides a developmental perspective to understand hypothalamus plasticity and obtain valuable insights into hypothalamic diseases such as anorexia, narcolepsy, and insomnia.

RESULTS

Transcriptional profiling of the developing hypothalamus

Rax-CreER^{T2} mice have recently been used to label hypothalamic primordium at early embryonic stages (Pak et al., 2014). To infer the lineage progression underlying hypothalamus development, we first labeled hypothalamic neuroepithelium by applying a single dose of tamoxifen to *Rax-CreER^{T2}::Ai14* mice at embryonic day 9 (E9) and performed lineage tracing (Figures S1A). Nearest-neighbor distance analysis of tdTomato⁺ cells 1 day after induction showed that the nearest cell-cell distance peaked at ~5 μm and did not exceed 20 μm (Figures S1B and S1C), suggestive of the homogeneous recombination without significant bias. Next we collected live tdTomato⁺ hypothalamic cells by fluorescence-activated cell sorting from induced *Rax-CreER^{T2}::Ai14* mice across 4 different time points (E11, E14, post-natal day 0 [P0] and P7) for single-cell RNA sequencing (Figures 1A and S1D; Mendeley Figures S1A and S1B). A final dataset of 43,261 Rax-derived hypothalamic cells, covering an average of 11,376 unique molecular identifiers (UMIs) and 3,753 genes per cell, was obtained after quality control and batch integration (Figures S1E–S1I).

To determine the major cell types in the developing hypothalamus, we employed the uniform manifold approximation and projection (UMAP) method for dimensionality reduction to cluster cells, which stratified cells by their developmental timing and identities (Figures 1B and 1C; Mendeley Figure S1C). Map-

ping well-established markers genes onto the UMAP representation identified 8 principal cell types and 11 cell clusters: RGCs (*Vim*⁺), IPCs (*Ascl1*⁺ or *Neurog2*⁺), glutamatergic neurons (GLUs; *Tubb3*⁺*Slc17a6*⁺), GABAergic neurons (GABAs; *Tubb3*⁺*Slc32a1*⁺), astrocytes (ASs; *Aldh1l1*⁺), oligodendrocyte precursor cells (OPCs; *Olig1*⁺*Pdgfra*⁺), oligodendrocytes (ODs; *Mbp*⁺) and ependymal cells (ECs; *Foxj1*⁺) (Figures 1C and 1D; Mendeley Figure S1D). Notably, a cluster of RGCs encompassed *Col23a1*⁺ tanyocytes (TCs) born at the postnatal stage (Altman and Bayer, 1978; Chen et al., 2017). The identity of cell clusters was further confirmed by a set of cell-type-specific genes ascertained by differential gene expression analysis (Figure S1J; Table S1). By aligning our dataset with a single-cell hypothalamic atlas (Romanov et al., 2020), we showed that our data not only covered all hypothalamic cell types but also captured early RGCs and IPCs from E11 brains (Figure S1K), which are fundamentally important for analyzing the lineage progression of neural progenitors.

As expected, prenatal cells mainly featured the process of cell division, pattern specification, neuron differentiation, axogenesis, and axon guidance, whereas postnatal cells were characterized by neuronal apoptosis, gliogenesis, myelination, synapse organization, and maturation (Figure S1L). Temporal analysis of cell type proportion also corroborated the general rule that neurogenic processes precede gliogenesis (Figure S1M). Using Monocle 3 because of its optimization for large datasets and complex, potentially disjointed trajectories (Cao et al., 2019), we performed a pseudotemporal analysis to reconstruct the developmental trajectory of the hypothalamus across the entire cell lineage. Indeed, the multibranched cellular trajectory showed multipotential differentiation of founder cells into GABAs, GLUs, OPCs, ASs, TCs, and ECs (Figure 1E). We further subdivided all cells into neuronal and glial lineages for simplified trajectory inference using Monocle 2 (Qiu et al., 2017; Trapnell et al., 2014). The neuronal lineage analysis uncovered a simple continuous trajectory connecting RGCs, IPCs, and neurons, whereas the pseudotemporal ordering of glial lineage cells indicated multifurcation of RGCs into three branches: the OPC-OD, AS, and TC-EC sublineages (Figures 1F and 1G). We combined cluster and trajectory analyses to stratify neural cell types and unravel the developmental dynamics of hypothalamic cells.

Temporal dynamic analysis of RGCs reveals the embryonic origin of postnatal TCs

To dissect the diversity among prenatal RGCs and postnatal RGC-like cells in the hypothalamus, we subsetted all RGC clusters across different time points, regressed out cell cycle scores, and identified 11 subclusters of cells (Figures 2A, S2A, and S2B). Although the majority of RGCs were in G1 phase, three subclusters of RGCs displayed distinguishable cell cycle features, implying their entry into special cell states (Figures S2B and S2C). Using the expression pattern of lineage- and cell-type-specific marker genes, we assigned a single identity to each cluster and subdivided the RGCs into two major subpopulations: RGCs in a cycling, quiescent, or transitional state without lineage preference (cRGCs, qRGCs, or tRGCs, respectively) and RGCs entering the primitive state of lineage differentiation toward IPCs, OPCs, AS precursors (APs), ECs, or TCs (pri-IPCs,

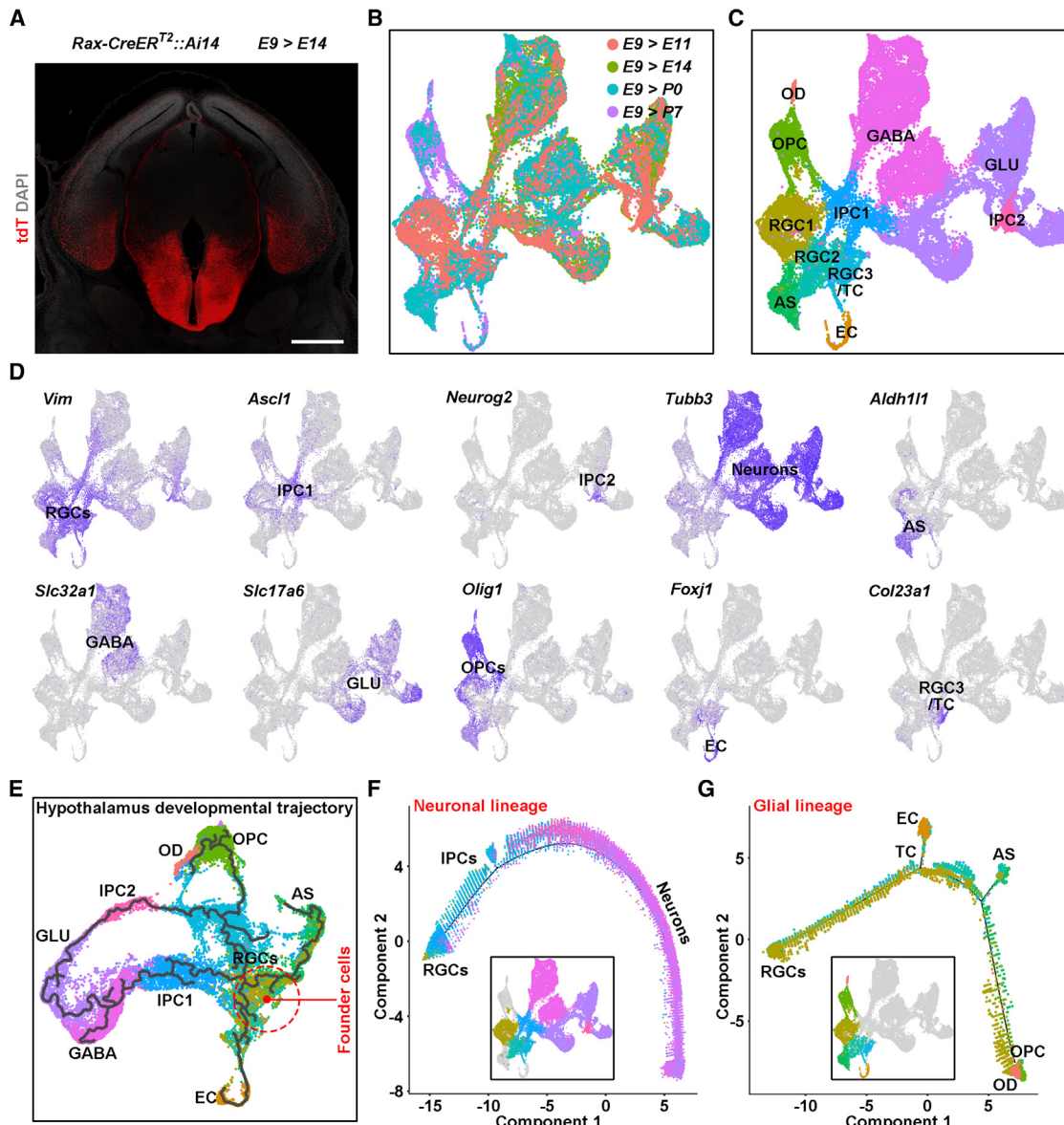


Figure 1. Molecular developmental trajectory of the mouse hypothalamus

(A) Representative image showing the genetically mediated fluorescent labeling of the hypothalamic cell lineage with *Rax-CreER^{T2}::Ai14* mice. The mice were induced with tamoxifen at a single dose of 132 mg/kg body weight at E9 and collected at E14. Scale bar, 500 μ m.

(B and C) UMAP visualization of 43,261 hypothalamic cells derived from *Rax⁺* neuroepithelium, colored by age (B) and groups (C). Hypothalamic cells were induced at E9 in *Rax-CreER^{T2}::Ai14* mice and collected at E11, E14, P0, and P7 for cell collection. The identities of cell groups are annotated according to known cell types. RGC, radial glial cell; IPC, intermediate progenitor cell; TC, tanyocyte; EC, ependymal cell; AS, astrocyte; OPC, OD precursor cell; OD, oligodendrocyte; GABA, GABAergic neuron; GLU, glutamatergic neuron.

(D) Imputed gene expression of canonical markers overlaid on the UMAP plot.

(E) Global developmental architecture of hypothalamic cell lineages inferred by Monocle 3. Shown is the trajectory of 11 cell clusters with 2,000 randomly subsampled cells. A red dashed circle indicates the potential founder cells.

(F and G) Pseudotemporal trajectories of the neuronal lineage (F) and glial lineage (G) in hypothalamus. The colored cells within boxed UMAP plots were used for imputing developmental trajectories.

pri-OPCs, pri-APs, pri-ECs, and pri-TCs, respectively) (Figures 2A and S2D; Table S2; Mendeley Figure S2). The trajectory inference with Monocle 3 and partition-based graph abstraction (PAGA) further identified cRGCs as the major founder cells to transform into RGCs with lineage preference for IPCs, OPCs, APs, and TCs-ECs (Figures 2B and S2E; STAR Methods).

Hypothalamic TCs, a specialized type of ECs, have recently been considered postnatal NSCs in the adult mammalian brain (Kokoeva et al., 2005; Lee et al., 2012). Although “set aside” and “continuous” models have been proposed to interpret the identity of precursors to adult NSCs in lateral ventricles and the hippocampus (Berg et al., 2019; Fuentealba et al., 2015),

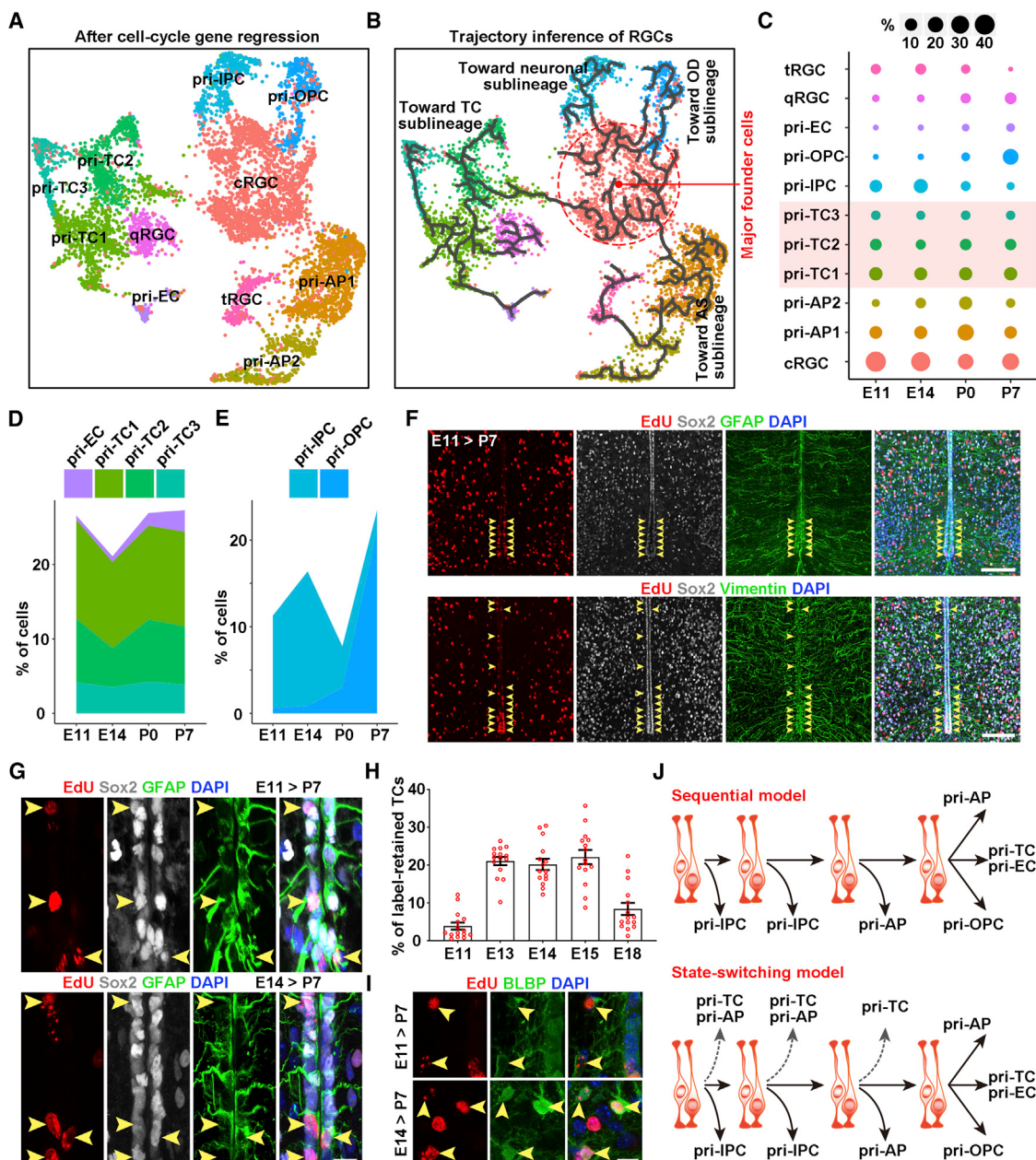


Figure 2. Strategically conserved RGCs switch to quiescence as a reservoir for hypothalamic TCs

(A) UMAP visualization of 11 clusters of hypothalamic RGCs after cell cycle gene regression, colored by cell subtypes/states and annotated based on expression of putative markers. cRGC, cycling RGC; qRGC, quiescent RGC; tRGC, transitional RGC; pri-IPC, primitive IPC; pri-OPC, primitive OPC; pri-TC, primitive TC; pri-EC, primitive EC; pri-AP, primitive AS precursor.

(B) Pseudotemporal trajectory of RGCs overlaid on the UMAP representation. The branched trajectory shows the differentiation of founder cells into neuronal, astroglial, OD and TC sublineages. A red dashed circle indicates the starter cells.

(C) The proportion of each RGC subtype at four developmental time points. The fractions of three pri-TC subtypes are highlighted in light red.

(D and E) Temporal dynamics of the proportion of RGC subtype committed to TC (D) or neuronal and OD sublineages (E).

(F) Sample confocal images showing EdU⁺ cells co-stained for the TC markers Sox2, GFAP, and Vimentin along the third ventricle. The animals were pulsed with a single dose of EdU at E11 and sacrificed at P7 for analysis. Yellow arrowheads indicate EdU⁺Sox2⁺GFAP⁺ or EdU⁺Sox2⁺Vimentin⁺ triple-labeled cells. Scale bars, 100 μm.

(G) Magnified images showing EdU⁺ TCs pulsed at E11 or E14 and chased at P7. Yellow arrowheads mark triple-labeled cells. Scale bar, 10 μm.

(H) Quantification of the ratio of label-retained TCs from animals receiving an EdU injection at different embryonic stages. Values represent mean ± SEM ($n = 15$ sections from 3 independent animals).

(I) Representative images showing staining for EdU and BLBP in P7 hypothalamus from mice receiving a single EdU pulse labeling at E11 (top) or E14 (bottom). EdU⁺BLBP⁺ label-retaining APs are indicated by arrowheads. Scale bar, 10 μm.

(J) Schematics of the traditional “sequential” model and our “state switching” model.

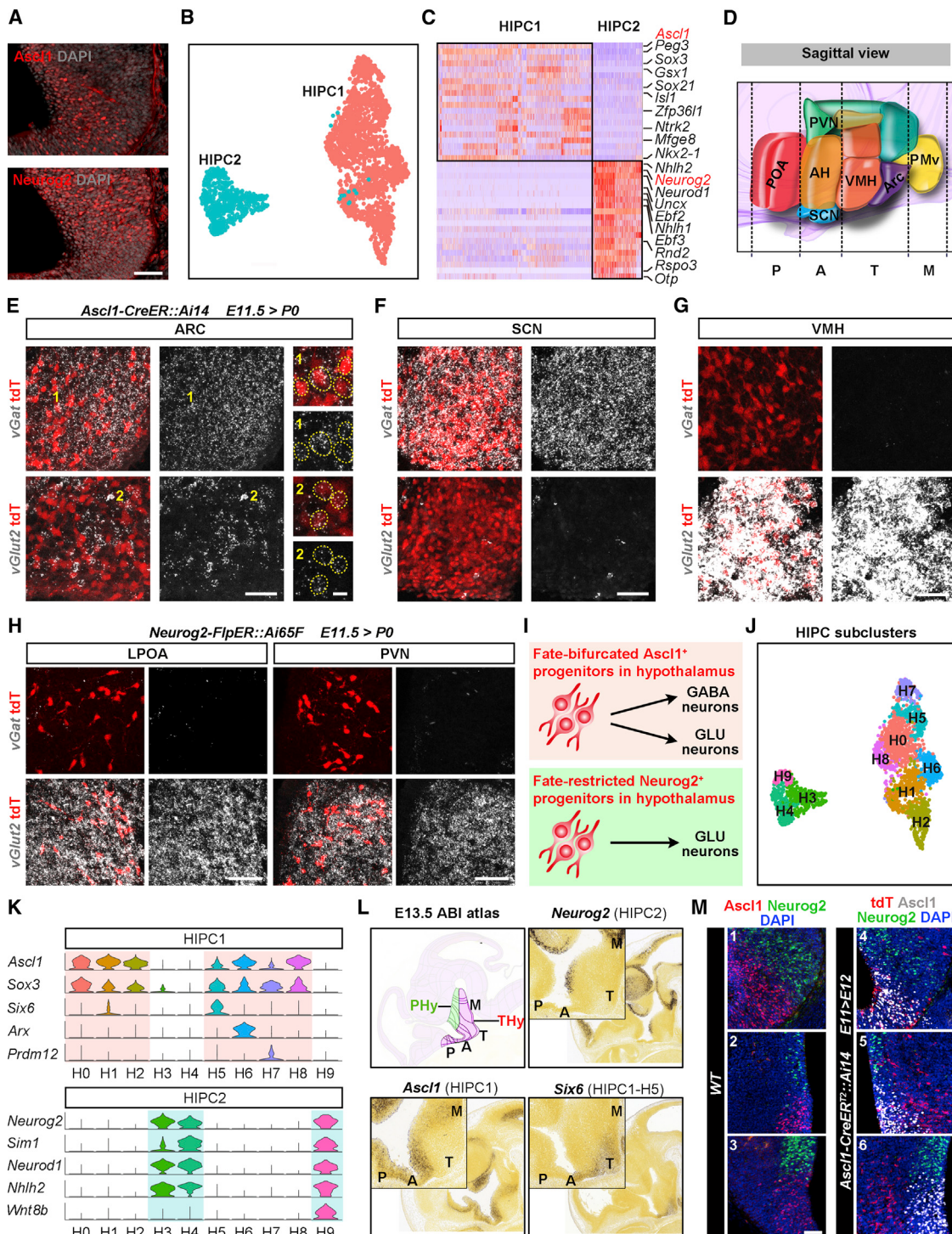


Figure 3. Fate diversification of two subpopulations of IPCs

(A) Immunostaining showing co-existence of Ascl1⁺ and Neurog2⁺ HIPC cells in the E11 hypothalamus. Scale bar, 50 μ m.

(B) UMAP plot of two main subpopulations of hypothalamic IPCs (HIPCs).

(C) A heatmap of genes expressed differentially in the Ascl1⁺ HIPC1 and Neurog2⁺ HIPC2 groups.

(D) Schematic showing a sagittal view of a developing hypothalamus traversing the preoptic (P), anterior (A), tuberal (T), and mammillary (M) zones. POA, preoptic area; AH, anterior hypothalamus; SCN, suprachiasmatic nucleus; VMH, ventromedial nucleus; ARC, arcuate nucleus; PMv, ventral premammillary nucleus; PVN, paraventricular nucleus.

(legend continued on next page)

the embryonic origin of hypothalamic TCs remains unclear. Our temporal analysis of cell type proportion showed that the percentage of various pri-TCs did not increase postnatally but remained constant during the developmental continuum (Figures 2C and 2D), implying that a subpopulation of RGCs starts to switch into precursors of TCs at early developmental stages. In contrast, the temporal dynamics of pri-IPC and pri-OPC proportions indicated predominantly prenatal neurogenesis and a postnatal surge in oligodendroglogenesis (Figure 2E). To validate the early-state switch from naive RGCs to pri-TCs, we applied a single dose of ethynyldeoxyuridine (EdU) into timed pregnant mice at different embryonic stages and performed a label retention assay at P7. Indeed, the birth dating analysis showed that a subset of RGCs exited the cell cycle and switched to the TC fate, marked by Sox2/Vimentin/GFAP (glial fibrillary acidic protein) and positioned along the third ventricle, as early as E11 (Figures 2F and 2G). Quantitative analysis indicated that the majority of TCs were derived from animals injected with EdU between E13 and E15 (Figure 2H). Likewise, a subpopulation of BLBP⁺ brain lipid-binding protein APs in hypothalamic parenchyma were born before E14 (Figure 2I). Therefore, our results support a “state-switching” model where a substantial fraction of TCs is derived from embryonic RGCs in parallel to prenatal neurogenesis rather than the “sequential” model, where RGCs sequentially produce neurons and glia and terminally differentiate into TCs (Figure 2J).

Hypothalamic RGCs give rise to differential IPC subpopulations

IPCs act as secondary, transient-amplifying neural progenitor cells, enabling rapid neurogenesis in the developing brain (Kowalczyk et al., 2009). In the telencephalon, neurogenic IPCs producing excitatory and inhibitory neurons arise from RGCs residing in dorsal and ventral pallium, respectively (Marín and Müller, 2014). To investigate the potency of hypothalamic RGCs in immediate progeny production, we extracted cells in the neuronal lineage at E11 to conduct pseudotemporal analyses using Monocle and scVelo. The developmental trajectory showed that RGCs bifurcated into two IPC sublineages for generating neurons within the hypothalamic niche (Figures S2F–S2H), suggesting that the starter cells initiate a lineage program to drive neurogenesis through two distinct types of IPCs. Population lineage tracing with *Rax-CreER*^{T2::Ai14} mice confirmed that hypothalamic RGCs indeed produced Ascl1⁺ and Neurog2⁺ IPCs (Figure S2I).

Two subpopulations of IPCs with distinct molecular profiles, lineage differentiation, and spatial distribution

The proneural factors Ascl1 and Neurog2 have been found previously to promote neuronal differentiation of progenitor cells and induce distinct neuronal subtype identities, specifying the fate of GABAs and GLUs in the telencephalon, respectively (Aydin et al., 2019; Fode et al., 2000; Parras et al., 2002). Here we identified two subpopulations of hypothalamic IPCs (HIPCs), defined by Ascl1 and Neurog2, respectively (Figures 1C and 1D), and revealed the coexistence of Ascl1⁺ and Neurog2⁺ progenitor cells in the developing hypothalamus (Figure 3A). After subsetting all HIPCs and regressing out cell cycle variation, we reclustered the cells and further compared the molecular profiles between the two main groups of HIPCs (Figures 3B, 3C, and S3A–S3C). Our data showed that HIPC1 and HIPC2 featured distinct sets of transcription factors (TFs): *Ascl1*, *Sox3*, *Gsx1*, and *Isl1* cooperated to define the identity of HIPC1, whereas *Neurog2* cooperated with *Nhlh2*, *Neurod1*, and *Otp* to govern HIPC2 identity (Figure 3C). Moreover, we found that HIPC1 and HIPC2 shared the enriched gene sets involved in neuronal fate specification, whereas they displayed differentially enriched cellular components even before differentiating into neurons, with HIPC1 expressing genes related to synapse formation for neuronal input and HIPC2 expressing genes associated with axonal growth for neuronal output (Figure S3D).

Although UMAP shows that HIPC2 was restricted within the GLU sublineage (Figures 1C, S2G, and S2H), the contiguity of HIPC1 with multiple neuronal sublineages raised questions regarding the fate of Ascl1⁺ IPCs in the hypothalamus. Hence, we conducted lineage tracing using *Ascl1-CreER*^{T2::Ai14} mice with tamoxifen induction at E11.5 to examine the fate specification of HIPC1 (Figure S3E). Single-molecule fluorescence *in situ* hybridization (smFISH) analysis revealed that Ascl1⁺ HIPCs contributed to generation of GABA (marked by vGat) and GLU (marked by vGlut2) subtypes in multiple hypothalamic nuclei (Figures 3D–3G and S3F–S3I), suggesting that Ascl1⁺ HIPCs are fate bifurcated in neuronal differentiation. To validate the fate specification of HIPC2, we generated *Neurog2-FlpER*^{T2::Ai65F} mice, performed lineage tracing, and found that Neurog2⁺ IPCs predominantly produced GLU subtypes in diverse nuclei (Figures 3H, 3I, and S3J–S3L).

To further explore the distinct lineage differentiation of HIPC1 and HIPC2, we traced these two IPC subpopulations and mapped the fate of their progeny neurons by immunostaining or smFISH. Although *in silico* analysis roughly subdivided

(E) Combination of smFISH and immunostaining shows that Ascl1⁺ HIPC1 gives rise to vGat⁺ GABA and vGlut2⁺ GLU progeny in the ARC. *Ascl1-CreER*^{T2::Ai14} mice were induced with tamoxifen at E11.5 and sacrificed at P0 for analysis. The numbered, magnified images show colocalization of tdTomato with vGat or vGlut2 at single-cell resolution. Scale bars, 50 μm and 10 μm (magnified images).

(F and G) Sample images showing generation of pure vGat⁺ neurons in the SCN (F) and vGlut2⁺ neurons in the VMH (G) by Ascl1⁺ HIPC1 subtype. Scale bars, 50 μm.

(H) Sample images showing predominant production of vGlut2⁺ neurons in the lateral POA (LPOA) and PVN by Neurog2⁺ HIPC2. *Neurog2-FlpER*^{T2::Ai65F} mice were induced with tamoxifen at E11.5 and sacrificed at P0 for analysis. Scale bars, 50 μm.

(I) Models summarizing the fate bifurcation of Ascl1⁺ IPCs and specific differentiation of Neurog2⁺ IPCs in the hypothalamus.

(J) Subclustering of two main subpopulations of HIPCs.

(K) Violin plots showing representative genes expressed specifically in HIPC1, HIPC2, or their subtypes.

(L) *In situ* hybridization of sagittal sections from E13.5 mouse brains, indicating the differential spatial distribution between HIPC1 and HIPC2. The hypothalamic region is magnified and shown in the top left corner. PHy, peduncular hypothalamus; THy, terminal hypothalamus; ABI atlas, Allen Brain Atlas.

(M) Immunostaining showing the mutually exclusive expression pattern of Ascl1 and Neurog2 in E12 hypothalamus from wild-type (WT, left) and *Ascl1-CreER*^{T2::Ai14} mice (right). *Ascl1-CreER*^{T2::Ai14} mice were induced at E11 and sacrificed at E12 for analysis. Scale bar, 50 μm.

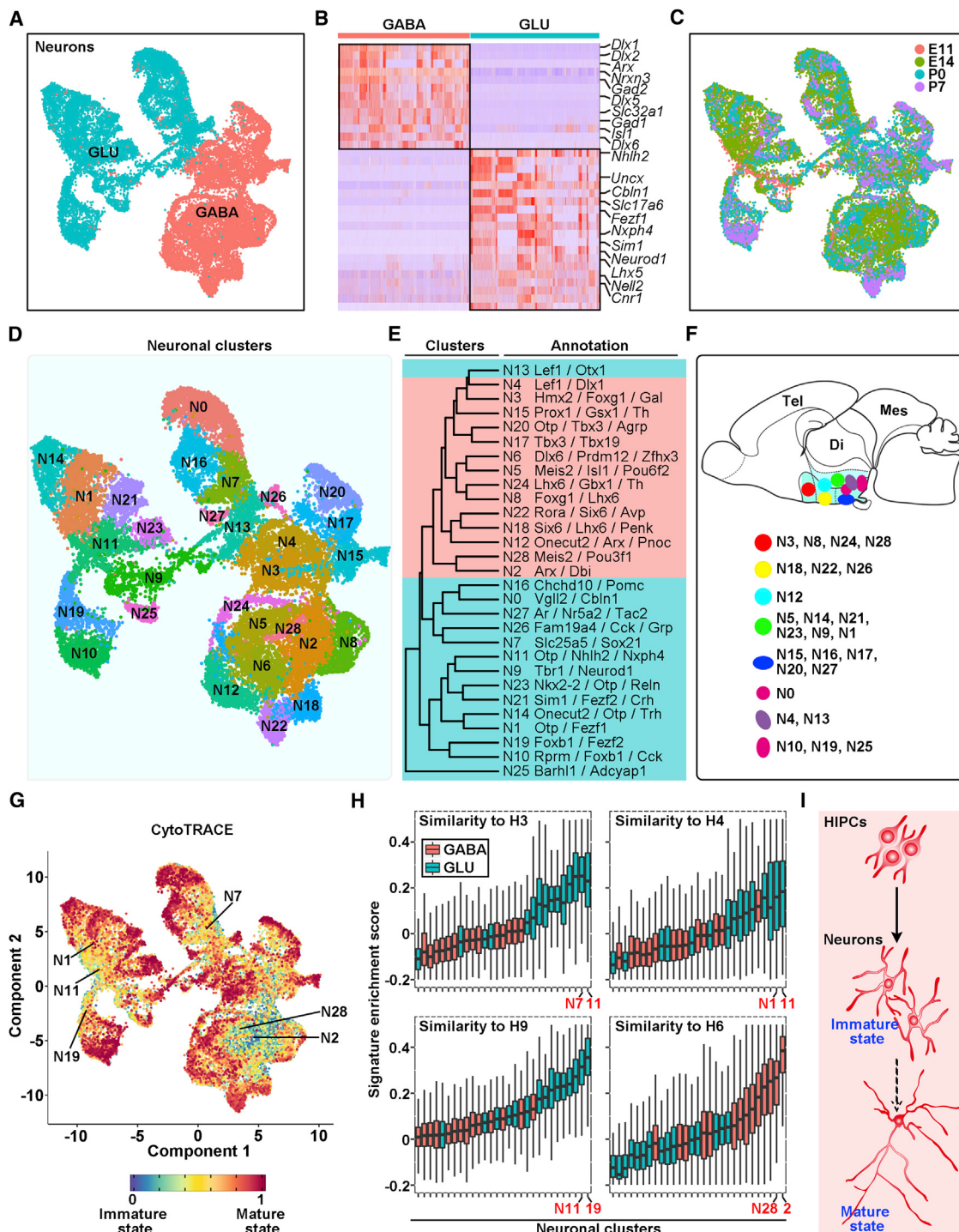


Figure 4. Subtypes and states of postmitotic neurons in the developing hypothalamus

- (A) UMAP plot showing the two main groups of hypothalamic neurons distinguished by fast neurotransmitters.
- (B) Heatmap of genes expressed differentially in GABA and GLUs in the developing hypothalamus.
- (C) UMAP representation of postmitotic neurons, colored by their developmental stages.
- (D) Subclustering of neurons into 29 subtypes, including 14 GABAergic and 15 glutamatergic subgroups.
- (E) Characterization and annotation of neuronal subtypes. The dendrogram shows the transcriptional relatedness of neuronal subtypes, annotated by combinatorial molecular codes of transcription factors (TFs) and/or neuropeptides.
- (F) Schematic showing the spatial orientation of distinguishable neuronal subtypes.
- (G) Maturation state of developing hypothalamic neurons predicted by CytoTRACE and overlaid on the UMAP representation. Six clusters of neurons at relatively nascent states are labeled.

(legend continued on next page)

HIPC1-derived cells into 4 groups positive for *Nr5a1/Sox14*, *Otp^{ARC}*, *Hmx3*, and *Dlx1*, our experimental results confirmed that Ascl1⁺ IPCs generated these 4 cell groups but not Foxb1⁺ cells (Figure S4A). Within the arcuate nucleus (ARC), Ascl1⁺ IPCs gave rise to multiple peptidergic neurons (Figure S4B). In parallel, we also examined the fate of HIPC2 and found that Neurog2⁺ IPCs produced 3 main cell subpopulations positive for *Tbr1*, *Foxb1*, and *Otp/Fezf1/Cbln1^{PVN/SON}* (Figure S4C). These data demonstrate a dichotomy between HIPC1 and HIPC2 in their lineage specification.

We next sought to investigate the spatial distribution of distinct HIPC subpopulations in the embryonic hypothalamus. Reclustering analysis at higher resolution yielded 7 subclusters (H0–H2 and H5–H8) for HIPC1 and 3 subclusters (H3, H4, and H9) for HIPC2, and UMAP-based trajectory inference suggested that the IPCs in the H0–H2 and H8 subgroups represented a more primitive state than the cells in the H5–H7 subclusters, confirmed by expression analysis of stemness genes (*Sparc*, *Slc1a3*, and *Apoe*) (Figures 3J and S5A–S5D; Table S3; Mendeley Figure S3). To explore the different spatial codes of HIPC1 and HIPC2, we cross-referenced the markers with *in situ* hybridization data from the Allen Developing Mouse Brain Atlas (Figures 3K, 3L, and S5D). The hypothalamus has traditionally been subdivided into peduncular and terminal regions along the longitudinal axis and the preoptic, anterior, tuberal, and mammillary zones along the sagittal axis. Here we found that Neurog2⁺Sim1⁺ HIPC2 was spatially restricted within the peduncular region and mammillary zone, whereas Ascl1⁺Sox3⁺ HIPC1 exhibited much more widespread distribution in the preoptic, anterior, and tuberal zones (Figures 3L and S5D). In particular, the H5–H7 subclusters, representing a predifferentiated state, spanned the anterior to tuberal zones (Figures 3L, S5B, and S5D). To corroborate the different spatial distribution of HIPC1 and HIPC2, we co-stained Ascl1 and Neurog2 in early embryonic brains and found that these two proneural factors were largely expressed in a complementary manner in the hypothalamus at E11 and E12 (Figures 3M, S5E, and S5F). Moreover, fate mapping analysis showed that Ascl1-derived cells differentiated rapidly and migrated toward the marginal stratum with little overlap with Neurog2⁺ IPCs (Figures 3M, S5G, and S5H). Our results reveal the different molecular and spatial codes of two subpopulations of IPCs, which may instruct their diversified lineage differentiation in the hypothalamus.

Hypothalamic neuronal subtypes and their regulons for specifying subtype identities

To taxonomize the neuronal subtypes in the developing hypothalamus, we extracted all postmitotic neurons and subdivided them into two major neuronal classes: 13,349 GLUs and 13,658 GABAs (Figure 4A). In the neocortex, Dlx homeobox TFs are required for GABAergic interneuron production, and, in contrast, another four TFs (*Fezf2*, *Ctip2*, *Tbr1*, and *Satb2*) regulate the cell fate acquisition of glutamatergic cortical neurons (Leone et al., 2008; Petryniak et al., 2007). Notably, although

Dlx factors, including *Dlx1*, *Dlx2*, *Dlx5*, and *Dlx6*, were also enriched in differentiated GABAs, another set of TFs, such as *Nhlh2*, *Uncx*, *Fezf1*, and *Lhx5*, showed class-specific expression in GLUs in the developing hypothalamus (Figure 4B), suggesting that cortical and hypothalamic neurons could adopt a comparable TF code to specify inhibitory neurons but different TF codes to drive differentiation of excitatory neurons.

We subsequently analyzed the spatiotemporal organization of hypothalamic neurons. Along the temporal trajectories, the transcriptional programs of both neuronal classes changed from neuronal differentiation and pattern specification to synapse organization, neurotransmitter release, and hormone secretion (Figures 4C and S6A–S6F). We further cataloged 29 neuronal subtypes with an unsupervised clustering approach, used a combinatorial code of TFs and neuropeptides to define the identity of each cluster, and linked the molecularly defined cell subtypes to their spatial distribution in diverse hypothalamic nuclei (Figures 4D–4F and S6G; Table S4; Mendeley Figures S4 and S5). For example, neuronal clusters N3, N8, N24, and N28 were spatially segregated in the preoptic area (POA; Mendeley Figure S4A).

Moreover, we applied cellular trajectory reconstruction analysis using gene counts and expression (CytoTRACE) and Monocle to decipher the degree of differentiation of all neuronal subtypes (Gulati et al., 2020) and found a “central-to-peripheral” maturation pattern in GABAs and GLUs (Figures 4G and S6H–S6J). Scoring of 29 neuronal subtypes with the molecular signatures of all HIPC subgroups indicated that GLU clusters bore closer resemblance to HIPC2 subgroups (H3, H4, and H9) and that the neuronal subtypes with higher scores tended to be immature cells (Figures 4H and S6K–S6M; Mendeley Figure S6). These results suggest that our dataset covers a continuum of neurons in immature and mature states (Figure 4I). We provide a comprehensive atlas of developing hypothalamic neurons with different molecular profiles, spatial distributions, and maturation degrees.

We proceeded to explore the subtype-specific TFs and their essential roles in organizing the gene-regulatory networks (i.e., regulons) that determine the fate of each neuronal subtype. We first screened 4,482 transcriptional regulators and identified 191 TFs with specific expression in different neuronal subtypes (Figures 5A; Table S5). It has been reported previously that core sets of TFs act together in a regulated manner to control gene expression and shape cellular identities (Chen et al., 2008; Hobert, 2004; Shirasaki and Pfaff, 2002). We performed a co-expression modular analysis and found 15 TF modules that may function synergistically to define neuronal subtype identities (Figure 5B). We exemplified TF module 11, in which *Lmx1a*, *Irx5*, *Pitx2*, *Barhl1*, and *Foxa1* displayed a significant association. A recent report has demonstrated that *Lmx1a*, *Pitx2*, and *Barhl1* are co-expressed in most neurons in the subthalamic nucleus (STN) and exhibit permutations of co-expression in other hypothalamic GLUs (Kee et al., 2017). Our data validated co-expression of *Lmx1a* and *Irx5* in multiple nuclei and confirmed

(H) Boxplots showing the gene set enrichment scores of HIPC molecular signatures for each neuronal subtypes. Boxes represent the interquartile range, and whiskers represent the minimum and maximum values. The top 2 neuronal subtypes with the highest scores, showing a transcriptional similarity to 4 HIPC subgroups, are labeled for each boxplot.

(I) Schematic showing that differentiation of hypothalamic neurons requires a transition from a nascent to a mature state.

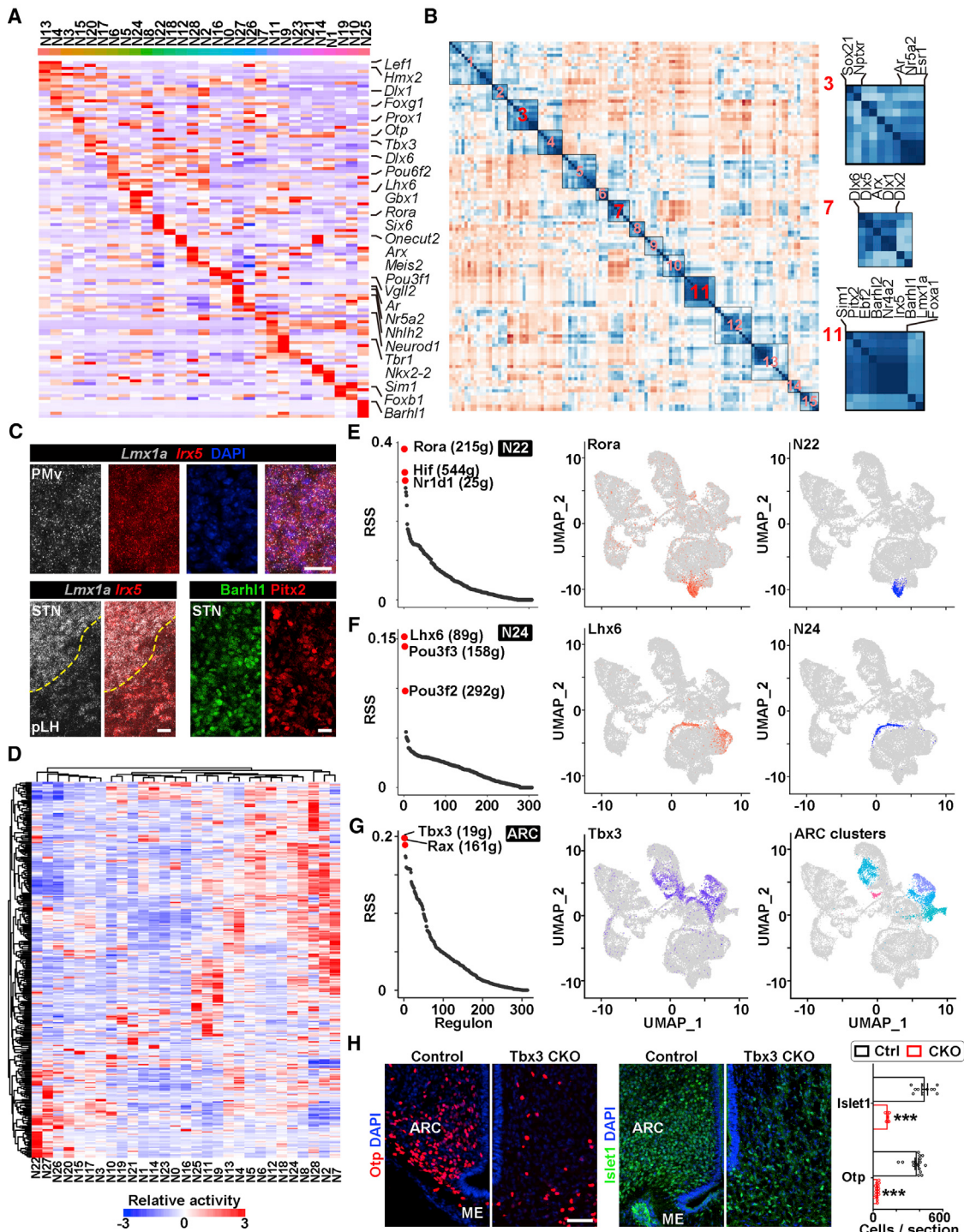


Figure 5. Molecular determinants of neuronal subtype identity

- (A) A heatmap of 191 subtype-specific TFs expressed in hypothalamic neurons.
- (B) Matrix showing the 15 TF modules with correlated expression patterns. Modules 3, 7, and 11 with potential regulatory interactions are highlighted.
- (C) Sample images showing colocalization of *Lmx1a* and *Irx5* mRNA transcripts and costaining of *Barhl1* and *Pitx2* proteins. pLH, posterior lateral hypothalamus; STN, subthalamic nucleus. Scale bars, 20 μm.
- (D) Heatmap showing the activity of 313 essential regulons for each neuronal subtype.
- (E and F) Shown are the ranked regulons for the N22 (E) and N24 (F) clusters and top regulon expression and UMAP visualization of the respective neuronal subtypes (from left to right). The top 3 regulons for each neuronal subtype are labeled, and the number of predicted target genes is shown in brackets.
- (G) Ranked regulons for ARC neuronal clusters and Tbx3 feature plot.

(legend continued on next page)

co-labeling of Barhl1 and Pitx2 in the STN (Figure 5C). To gain insight into the regulons underlying specification of individual nuclei and neuronal subtypes, we applied single-cell regulatory network inference and clustering (SCENIC), a computational tool for deciphering regulons, to map a regulatory network atlas (Aibar et al., 2017). We identified 313 regulons with strikingly enriched motifs for the master TFs by applying a *cis*-regulatory analysis to our single-cell dataset (Figure 5D), allowing us to determine the critical regulators for cell identity. We then assigned regulons to each neuronal subtype, ordered the regulons based on their regulon specificity score (RSS), and chose the top-ranked regulons for further analysis (Figures 5E, 5F, and S7A–S7D). To test the efficacy of this approach, we exemplified the neuronal subtypes distributed in the suprachiasmatic nucleus (SCN) and found that *Rora* and *Six6* emerged as the top regulons associated with N22 and N18 clusters (Figure 5E; Mendelley Figure S7A), coinciding with previous studies identifying *Rora* as a critical regulator of clock genes and *Six6* as a master regulator of neuronal fate in the SCN (Clark et al., 2013; Sato et al., 2004; Wen et al., 2020). We further showed the specific expression of top-ranked regulons in corresponding neuronal clusters (Mendelley Figure S7). We provide a taxonomy of developing hypothalamic neurons in a nascent or mature state and a list of regulons specifying their identity.

Moreover, we also identified nucleus-specific regulons by linking neuronal subtypes to their nuclear distribution and revealed that *Tbx3* might serve as a critical regulon specifying the ARC (Figures 5G and S7E). Indeed, *Tbx3* mRNA was specifically expressed in the ARC in postnatal mouse brains (Figure S7F). Importantly, region-specific deletion of *Tbx3* by breeding the *Nkx2.1-Cre* driver line with *Tbx3*^{FloxFloxB} mice caused absence of the ARC (marked by *Otp* and *Islet1*), loss of the median eminence (ME) in the hypothalamus, and concurrent ablation of *AgRP* (N20), *Pomc* (N16), *Tbx19* (N17), and *TH* (tyrosine hydroxylase, N15) neurons (Figures 5H and S7G), extending a recent finding that suggests critical involvement of *Tbx3* in defining the peptidergic identity of melanocortin neurons (Quarta et al., 2019). These results indicate important functional relevance of regulons in specifying nucleus and neuronal subtypes.

Fate diversification into peptidergic neurons during the maturation process

Hypothalamic neurons are traditionally classified based on fast neurotransmitters (e.g., glutamate and GABA), monoamines (e.g., dopamine), and neuropeptides, and feature complex neuronal subtype diversity (Hökfelt et al., 2000; Puelles et al., 2012). Here we found that, although the neuropeptide genes *Gal*, *Npy*, *AgRP*, *Avp*, *Penk*, and *Pnoc* were specifically expressed in GABAs, *Pomc*, *Cbln1*, *Tac2*, *Cck*, *ReIn*, *Trh*, *Crh*, and *Adcyap1* were enriched in GLUs (Figure 4E). To provide a systematic view of peptide expression, we examined a total of 100 neuropeptides and monoamines and identified 34 of them showing specific expression pattern in diverse neuronal subtypes (Figure 6A; Table S5). Further correlation analysis revealed 8 co-expression

modules at the cluster level (Figure 6B), implying co-release of multiple peptides and monoamines from a single neuronal subtype or a common lineage origin of multiple peptidergic neurons. To test this, we focused on three prominent peptide modules (M3, M4, and M7), evaluated their expression pattern, and performed pseudotemporal analysis of representative neuronal subtypes covering nascent and mature neurons. Our data showed three patterns of peptidergic neuron development: (1) the N15 subtype gave rise to neurons co-releasing *Gal*, *Ghrh*, and dopamine in the ARC, suggesting its fate to differentiate into a single subtype of peptidergic neurons (Figures 6C and 6D); (2) the N20 subtype differentiated into *AgRP/Npy* neurons or *Sst* neurons in the ARC, suggesting its fate bifurcation (Figure 6E); and (3) nascent neurons in the N21 subtype diversified into *Avp*, *Crh*, and *Oxt* neurons in the paraventricular nucleus (PVN) during their maturation process, suggesting its multifurcation in cell fate decisions (Figure 6F). Further analysis of N3, N13, N14, N16, N25, and N26 neuronal subtypes confirmed the potential fate diversification of relatively nascent neurons (Mendelley Figure S8). To experimentally validate this claim, we selected the N20 neuronal cluster, in which *Sst* nascent neurons first appear at E11 in the marginal stratum of the tuberal zone (Morales-Delgado et al., 2011), and took advantage of *Sst-Cre::Ai14* mice for fate mapping. Our data showed that *Sst*-expressing nascent neurons could diversify into *Sst* and *AgRP* neurons in postnatal brains (Figures 6G, 6H, and S7H). Our results support the theory that hypothalamic peptidergic neuronal subtypes transit through a postmitotic transcriptionally immature state to generate more complex neuronal diversity.

Fate multifurcation of single RGCs revealed by *in vivo* clonal analysis

To investigate whether neuronal diversity originates from individual RGCs, we set out to develop a single-cell lineage-tracing system in the mouse hypothalamus. Our previous reports demonstrated that MADM (mosaic analysis with double markers) reporter mice in combination with *CreER*^{T2} driver mice are a genetic tool for spatially and temporally specific clonal analysis of dividing neural progenitors (Wong et al., 2018; Xu et al., 2018). Here we induced hypothalamic clones in *Rax-CreER*^{T2::MADM-11} mice by applying a single dose of tamoxifen at E10 and collected brains at the perinatal stage for clonal analysis. The labeled RGCs gave rise to green/red (GR) clones generated by G2-X segregation of chromatids or yellow (Y) clones arising from G2-Z segregation (Figures 7A and S7I–S7L). *Rax*-derived clones were distributed predominantly in the hypothalamus and very sparse, with only 35% of positive hemispheres in mouse brains (Figure 7B). Quantification of clonal size showed that each hypothalamic RGC produced an average of 7.9 cells during the time window of our analysis (Figures 7C and 7D). Cellular composition analysis of postnatal clones collected from *Rax-CreER*^{T2::MADM-11} and *Gli1-CreER*^{T2::MADM-11} mice revealed that ~40% of hypothalamic clones contained neurons and glia, and the average proportion of neurons per

(H) Immunostaining and quantification of *Otp*⁺ and *Islet1*⁺ cells distributed in the acroterminal tuberal zone of the hypothalamus. ME, median eminence; Ctrl, control; CKO, conditional knockout. Values represent mean ± SEM ($n = 15$ sections from 3 brains; *** $p < 0.001$; two-tailed unpaired Student's t test). Scale bar, 50 μ m.

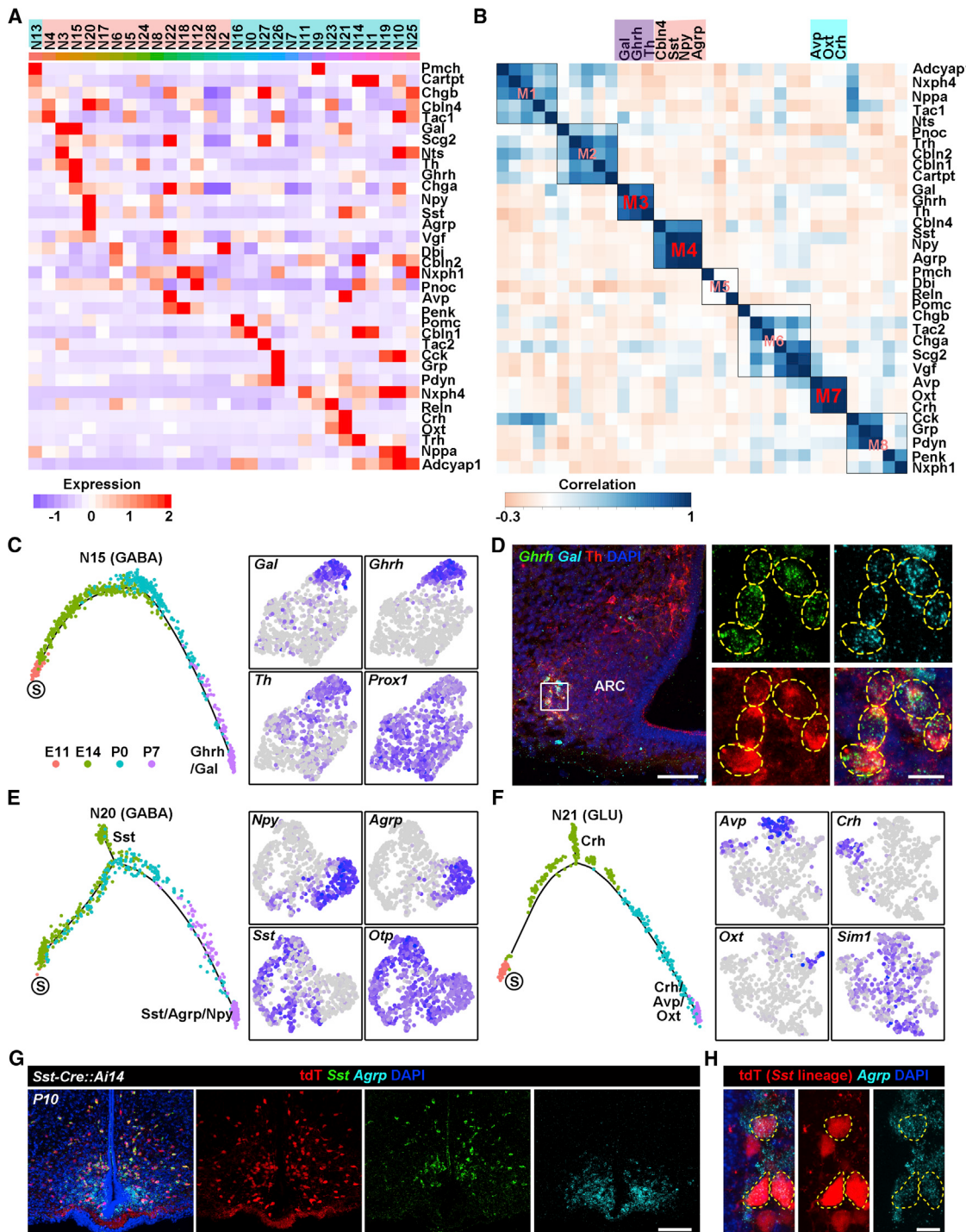


Figure 6. Developmental diversification of hypothalamic peptidergic neurons

(A) Heatmap showing 34 subtype-specific neuropeptides/monoamines expressed in hypothalamic neurons.

(B) Matrix showing the 8 neuropeptide/monoamine modules with correlated expression patterns. M3 (Gal, Ghrh, and Th), M4 (Cbln4, Sst, Npy, and AgRP), and M9 (Avp, Oxt, and Crh) modules display a significant correlation at the cluster level.

(C) Pseudotemporal trajectory of N15 neuronal subtypes specifically expressing M3 neuropeptide modules (left) and UMAP projection of the respective neuropeptide or TF expression (right). S, starter cells for lineage progression.

(D) Sample images showing co-labeling of Ghrh, Gal, and Th in a subpopulation of arcuate neurons in a P0 hypothalamus. smFISH was performed to detect Ghrh and Gal mRNA, followed by immunostaining of TH. The boxed area is magnified, and dashed circles indicate co-stained neurons. Scale bars, 100 µm (left) and 10 µm (right).

(legend continued on next page)

clone in the terminal region was significantly higher than clones in the peduncular region at the expense of glial production (Figures 7E and 7F). To investigate clonal organization, we sorted out RGC-retaining clones, exploited the radial processes of residual RGCs, exported 3D coordinates of clonally related cells, and analyzed the putative radial and tangential migration distance to elucidate the dispersion profiles of hypothalamic cells (Figure 7G). Reconstruction of perinatal and postnatal clones hinted that most hypothalamic clones were organized into non-radial clusters (Figures S7I–S7N), in contrast to the radial columns in the cortex. Our quantitative analysis showed that hypothalamic cells in the terminal region underwent longer tangential migration and shorter radial migration than those in the peduncular region (Figures 7H–7K), suggesting that terminal hypothalamic clones have a propensity to disperse more tangentially.

Given that the N20 cluster was found to contain at least two neuronal subtypes controlling feeding behavior and energy balance (Figure 6E; Campbell et al., 2017), we specifically selected clones with residual RGCs in proximity to the ARC to assess the capacity of RGCs in neuronal subtype specification and whether AgRP and SST neurons share the common origin at the single-progenitor level. As a proof of concept, we found that individual RGCs indeed generated AgRP, SST, and even POMC neurons in the “feeding center” (Figures 7L and S7O; Video S1). Hence, our results not only confirm the lineage relatedness between AgRP and SST neurons but also suggest generation of neuronal diversity by single RGCs during hypothalamus development.

DISCUSSION

Understanding the principles governing generation of neuronal diversity in complex brain structure and developmental specification programs contributing to this diversity is fundamentally important to dissect how neurons are assembled to form functional neural networks. Our single-cell transcriptomics analyses of cells spanning multiple developmental stages of hypothalamic neurons suggest a cascade diversification model where RGCs, HIPCs, and nascent neurons along the cellular hierarchy contribute to fate diversification of hypothalamic neurons in a step-by-step amplifying fashion, with each step under precise control of subtype-specific TFs. Our model supports the common developmental principle that generation of neuronal diversity relies on temporal and spatial patterning of neural progenitors (Holguera and Desplan, 2018; McConnell, 1991; Telley et al., 2019) but differs from the predetermined fate model, where cortical RGCs undergo asymmetric cell divisions to produce fate-specified IPCs with specific spatiotemporal coding, and the stochastic model, where retinal progenitor cells (RPCs) are subject to stochastic factors controlling neuronal fate specification (He et al., 2012; Kohwi and Doe, 2013). Given the extreme neuronal diversity in the hypothalamus, it is reasonable for hypothalamic progenitors to adopt a cascade diversification strategy

to yield extraordinary heterogeneity. A recent study provided a valuable dataset of the developing hypothalamus and identified a set of regulons shaping neuronal diversity (Romanov et al., 2020). However, this work did not capture early RGCs and IPCs for studying their lineage progression because of the lack of cells prior to the peak of hypothalamic neurogenesis at E12.5 (Ishii and Bouret, 2012). We not only uncovered production of two IPC subpopulations by hypothalamic RGCs and generic fate bifurcation of *Ascl1*⁺ HIPCs but also analyzed fate diversification of immature neurons during development, which collectively support the cascade diversification model. Our clonal analysis further provides a proof of concept to reveal the capacity of single RGCs in differentiating into multiple neuronal subtypes.

As the cells residing at the top of neural lineage hierarchy, multipotential RGCs lining the third ventricle exploit a conserved strategy to sequentially produce neuronal and glial lineages. In contrast to the striking regional specification of RGCs in the telencephalon, where the dorsal and ventral subdivisions contain different subpopulations of neural progenitors with diverse potential in neuronal fate decision (Guillemot, 2005; Parras et al., 2002), hypothalamic RGCs have the capacity to produce *Ascl1*⁺ and *Neurog2*⁺ IPCs that differentiate into GABAs and GLUs, respectively, in the neocortex (Aydin et al., 2019; Fode et al., 2000; Lo et al., 2002). We also showed that RGCs in the embryonic hypothalamus exit the cell cycle and switch to the pri-TC state at an early developmental stage and proposed a “state switching” hypothesis to interpret the embryonic origin of TCs. Recent studies have provided “set aside” and “continuous” models to depict the embryonic origin of adult NSCs in the lateral ventricles and hippocampus, respectively (Berg et al., 2019; Fuentealba et al., 2015). Although hippocampal RGCs continuously produce progeny until they transition to a quiescent state postnatally in the “continuous” model, the “set aside” and our “state switching” models suggest that RGCs stop dividing at similar embryonic stages and remain largely quiescent until the postnatal stage.

Ascl1⁺ and *Neurog2*⁺ IPCs coexist in the developing hypothalamus, constituting the second-tier cells of the neural lineage hierarchy and displaying different molecular profiles, spatial distribution, and lineage differentiation. Spatially, *Ascl1*⁺ and *Neurog2*⁺ progenitor domains are largely distributed in a complementary manner in the early embryonic hypothalamus. Although *Neurog2*⁺ HIPCs predominantly produce GLUs, *Ascl1*⁺ HIPCs can differentiate into GABAs and GLUs during their lineage progression, in contrast with the restriction of *Ascl1*⁺ IPCs to the GABAergic fate in the ventral telencephalon (Parras et al., 2002). Notably, *Mash1* (encoded by *Ascl1*) has been reported to be expressed in embryonic neural progenitors in the dorsal telencephalon and adult radial glial-like cells in the hippocampus (Britz et al., 2006; Pilz et al., 2018), both of which presumably produce GLUs. Combination of bioinformatics analysis with fate mapping of *Ascl1*⁺ and *Neurog2*⁺ IPCs further clarifies

(E and F) Trajectory of N20 and N21 clusters (left) and expression of M4 and M9 neuropeptide modules (right). *Otp* and *Sim1* were selected as pan-markers for N20 and N21 subtypes.

(G) Sample images showing expression of *Sst* or *AgRP* in *tdTomato*⁺ cells in the hypothalamus of P10 *Sst-Cre::Ai14* mice. *Sst* and *AgRP* mRNAs were detected by smFISH. Scale bar, 100 μm.

(H) Representative images showing that *Sst*-expressing cells give rise to *AgRP* neurons. Dashed circles indicate expression of *AgRP* in *Sst*-derived *tdTomato*⁺ cells. Scale bar, 10 μm.

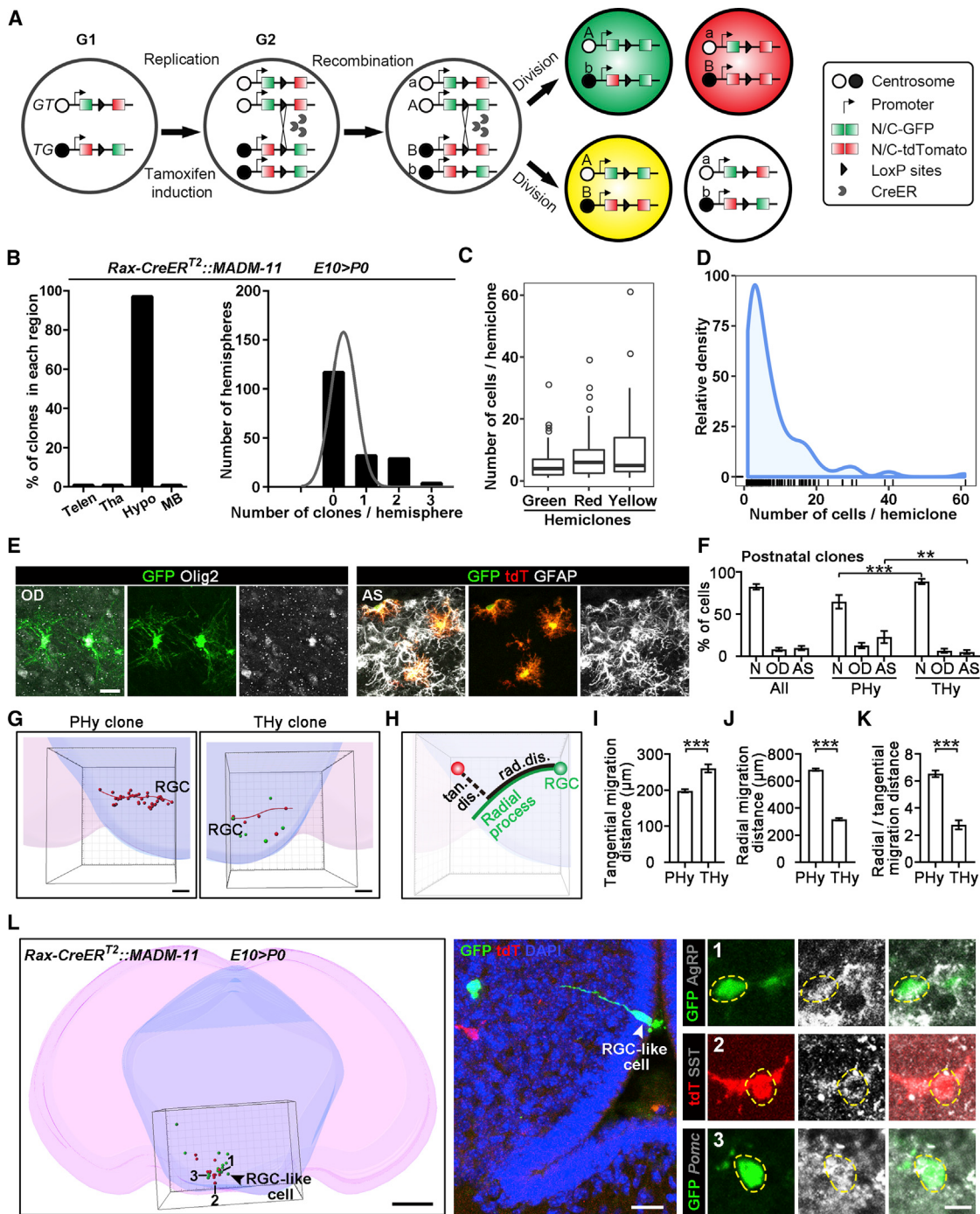


Figure 7. *In vivo* clonal analysis reveals generation of multiple neuronal subtypes by single RGCs

(A) MADM scheme.

(B) Summaries of the positioning of labeled clones in *Rax-CreER^{T2}::MADM-11* mice (left) and the number of clones per brain hemisphere (right). The curve represents the best non-linear fit. The mice were induced at E10 and sacrificed at P0 for analysis. Telen, telencephalon; Tha, thalamus; Hypo, hypothalamus; MB, midbrain.

(C) Boxplot showing clonal size in green (G), red (R), and yellow (Y) hemiclones ($n = 160$). Boxes represent the interquartile range (IQR), whiskers extend to ± 1.5 IQR, dots represent outliers, and bold black lines indicate median values.

(D) Density plot illustrating the distribution of the number of cells per hemiclone.

(E) Representative images of ODs with colocalization of GFP and Olig2 and ASs with costaining of GFP/tdTomato and GFAP in postnatal clones. Scale bar, 50 μm.

(F) Summary of the average number of neurons (N), ODs, and ASs in all ($n = 80$), PHy ($n = 21$), and THy ($n = 59$) clones from postnatal *Rax-CreER^{T2}::MADM-11* and *Gli1-CreER^{T2}::MADM-11* brains. Values represent mean \pm SEM (** $p < 0.01$, *** $p < 0.001$; one-way ANOVA).

(legend continued on next page)

their different neuronal lineage commitment *in vivo*. Interestingly, neurons derived from *Ascl1*⁺ HIPCs populate multiple hypothalamic nuclei, including the ventromedial nucleus (VMH), predominantly comprised of GLUs. It has been reported that *Ascl1* acts via *Neurog3* to specify VMH neuronal fate (Aslanpour et al., 2020), supporting the bipotency of *Ascl1*⁺ HIPCs in neuronal specification.

We further identified nascent postmitotic neurons as the third-tier cells contributing to generation of neuronal diversity in the hypothalamus. Compared with the molecular taxonomy of adult hypothalamic neurons (Campbell et al., 2017; Chen et al., 2017), our single-cell dataset contains immature neurons whose fates are flexible to be restricted, bifurcated, or multifurcated in neuronal specification. Given that there is rapid induction of neuropeptides in the mouse hypothalamus between P2 and P10 (Romanov et al., 2020), we combined pseudotemporal analysis with peptide expression to predict the fate specification of immature neurons among different neuronal sublineages and confirmed by lineage tracing that neurons at a nascent state are capable of resolving into multiple peptidergic neuronal subtypes. Consistent with our hypothesis that nascent neurons could be fate diversified during maturation, a recent study of the peripheral nervous system demonstrated that the divergent somatosensory neurons transition from an unspecialized state to transcriptionally diverse subtypes (Sharma et al., 2020). Moreover, we also detected a plethora of regulons potentially specifying the fate of diverse hypothalamic neuronal subtypes. The identified regulons, such as *Rora*, *Lhx6*, *Gsx1*, *Six6*, *Otp*, *Hmx3*, *Pou3f2*, and *Lhx2*, have been found previously to regulate hypothalamic neuronal fate commitment and physiological functions (Alvarez-Bolado, 2019; Xie and Dorsky, 2017). For nucleus specification, although previous studies have suggested that SF-1 and Six6 specify the VMH and SCN, respectively (Clark et al., 2013; Gao and Sun, 2016; Ikeda et al., 1995), the factor specifying the ARC formation was unclear. Here we show that genetic deletion of the nucleus-specific regulon *Tbx3* abolishes the ARC from the hypothalamus and concurrently ablates *Agrp*, *Pomc*, *Tbx19*, and TH neurons residing in the ARC.

We revealed a stepwise amplification strategy used by neural progenitors to yield extreme neuronal heterogeneity in an evolutionarily conserved brain structure. Disclosure of spatiotemporal patterning of hypothalamic neurogenesis at single-cell resolution provides key insights into the intrinsic nature of neural progenitors and their progeny to develop highly diverse subpopulations of neurons, although the role of environmental cues in shaping neuronal diversity requires further exploration. Our study will streamline future studies to generate individual hypothalamic neuronal subtypes *in vitro*, decipher functional microcircuits among hypothalamic neurons during development, and investigate the pathophysiological mechanisms underlying hypothalamic disease.

Limitations of study

There are certain limitations to the interpretation of our results. First, collection of our single-cell dataset relied on sorting of fluorescently labeled hypothalamic cells from induced *Rax-CreER-T2::Ai14* mice. Although we showed that there was no sampling bias, we could not guarantee 100% cell labeling efficiency. Second, although our clonal analysis results demonstrate fate multifurcation of individual RGCs, our cascade diversification model is largely built on the cellular hierarchy at the population level. For the following reasons, it remains challenging to define the peptidergic identity of sister neurons arising from a single IPC. (1) MADM-based clonal lineage tracing frequently labels a single neural progenitor per brain and is characterized by high resolution but extremely low throughput. (2) Our previous study suggested that labeling of IPCs is distributed randomly across the diencephalon, and a single IPC frequently produces only 2–4 neurons (Wong et al., 2018), which obstructs efficient evaluation of lineage relationships. (3) The hypothalamus consists of extremely heterogeneous peptidergic neurons, preventing us from precisely identifying the peptidergic identity of randomly labeled sister neurons. Nevertheless, we applied population lineage tracing to confirm that *Ascl1*⁺ and *Neurog2*⁺ IPCs generated multiple neuronal subtypes in the hypothalamus. Last, development of an inducible barcoding approach in combination with single-cell analysis is required to systematically decode the lineage relationships of diverse neuronal subtypes at the onset of hypothalamic neurogenesis.

STAR METHODS

Detailed methods are provided in the online version of this paper and include the following:

- KEY RESOURCES TABLE
- RESOURCE AVAILABILITY
 - Lead contact
 - Materials availability
 - Data and code availability
- EXPERIMENTAL MODEL AND SUBJECT DETAILS
- METHOD DETAILS
 - Tamoxifen Induction
 - EdU Pulse-Chase Assay
 - Single-Cell Isolation
 - Single-Cell RNA Library Preparation and Sequencing
 - EdU Staining and Immunohistochemistry
 - Single-molecule Fluorescent *In Situ* Hybridization (smFISH)
 - Cross-Reference of Allen Mouse Brain Atlas
 - Pre-Processing of Sequencing Data
 - Quality Control and Data Integration
 - Cell-Cycle Analysis

(G) Spatial organization of representative PHy and THy clones at P7. Spots with long radial processes indicate retained RGC-like cells. Scale bars, 400 μm.
(H) The method to scale the tangential and radial migration distance (tan. dis. and rad. dis., respectively).

(I–K) Quantification of tan. dis. (I) and rad. dis. (J) in each clone in the PHy and THy and summary of the ratio of the tangential and radial dispersion distance (K). Data are shown as mean ± SEM (**p < 0.001, two-tailed unpaired Student's t test).

(L) Three-dimensional reconstruction of a hypothalamic clone from P0 *Rax-CreER-T2::MADM-11* mice (left). Sample images show a residual RGC-like cell (center) and differentiation of a single RGC into AgRP, SST, and POMC neurons in the clone (right). AgRP and SST proteins were detected by immunostaining, whereas *Pomc* mRNA was examined by smFISH. Scale bars: 500 μm (left), 20 μm (center), and 10 μm (right).

- Dimensionality Reduction and Clustering
- Differential Gene Expression Analysis
- Monocle Pseudotemporal Analysis
- Gene Expression Signature Scoring
- RNA Velocity Analysis
- CytoTRACE Analysis
- Partition-based Graph Abstraction (PAGA) Analysis
- TF and Neuropeptide Modular Analysis
- Regulon Analyses for Neuronal Subtypes and Nuclei
- Clonal Analysis and Quantification
- **QUANTIFICATION AND STATISTICAL ANALYSIS**
 - General Statistical Analysis
 - Nearest Neighbor Distance Analysis

SUPPLEMENTAL INFORMATION

Supplemental information can be found online at <https://doi.org/10.1016/j.stem.2021.03.020>.

ACKNOWLEDGMENTS

We thank Yingqin Li, Samuel Wong, Xiaohong Xu, and Jie He for comments on the manuscript and Lan Jiang for intensive discussions. We gratefully acknowledge Dr. Zhengang Yang, Dr. Songhai Shi, Dr. Man Jiang, Dr. Peng Cao, and Dr. Anne Moon's laboratory for providing us diverse mouse strains for lineage tracing and functional study. The work was supported by the National Key R&D Program of China (2019YFA0801900 and 2018YFA0801104), the National Natural Science Foundation of China (31771131, 81891002, 31921002, and 32070972), the Strategic Priority Research Program of Chinese Academy of Sciences (XDB32020000), the Hundred-Talent Program (Chinese Academy of Sciences), and the Beijing Municipal Science & Technology Commission (Z181100001518001).

AUTHOR CONTRIBUTIONS

Q.-F.W. conceived and supervised the project. M.X. performed scRNA-seq experiments. Y.-H.Z. and H.W. performed the bioinformatics analysis. X.S., Y.-H.Z., M.X., X.-L.S., W.M., J.W., P.S., M.Y., L.G., and M.H. conducted mouse lineage tracing and prepared brain samples. M.X., X.-L.S., W.M., S.L., X.S., and Q.-F.W. performed immunohistochemistry, *in situ* hybridization, and imaging. X.S., X.-L.S., and Q.-F.W. performed clonal analysis. Q.-F.W. and Y.-H.Z. developed the theory and wrote the manuscript.

DECLARATION OF INTERESTS

The authors declare no competing interests.

INCLUSION AND DIVERSITY

We worked to ensure sex balance in the selection of non-human subjects. We worked to ensure diversity in experimental samples through the selection of the genomic datasets.

Received: November 13, 2020

Revised: March 2, 2021

Accepted: March 24, 2021

Published: April 21, 2021

REFERENCES

- Albar, S., González-Blas, C.B., Moerman, T., Huynh-Thu, V.A., Imrichova, H., Hulselmans, G., Rambow, F., Marine, J.C., Geurts, P., Aerts, J., et al. (2017). SCENIC: single-cell regulatory network inference and clustering. *Nat. Methods* 14, 1083–1086.
- Altman, J., and Bayer, S.A. (1978). Development of the diencephalon in the rat. III. Ontogeny of the specialized ventricular linings of the hypothalamic third ventricle. *J. Comp. Neurol.* 182, 995–1015.
- Alvarez-Bolado, G. (2019). Development of neuroendocrine neurons in the mammalian hypothalamus. *Cell Tissue Res.* 375, 23–39.
- Aslanpour, S., Rosin, J.M., Balakrishnan, A., Klenin, N., Blot, F., Gradwohl, G., Schuurmans, C., and Kurrasch, D.M. (2020). *Ascl1* is required to specify a subset of ventromedial hypothalamic neurons. *Development* 147, dev180067.
- Aydin, B., Kakumanu, A., Rossillo, M., Moreno-Estellés, M., Garippler, G., Ringstad, N., Flames, N., Mahony, S., and Mazzoni, E.O. (2019). Proneural factors *Ascl1* and *Neurog2* contribute to neuronal subtype identities by establishing distinct chromatin landscapes. *Nat. Neurosci.* 22, 897–908.
- Berg, D.A., Su, Y., Jimenez-Cyrus, D., Patel, A., Huang, N., Morizet, D., Lee, S., Shah, R., Ringeling, F.R., Jain, R., et al. (2019). A common embryonic origin of stem cells drives developmental and adult neurogenesis. *Cell* 177, 654–668.e15.
- Bergen, V., Lange, M., Peidli, S., Wolf, F.A., and Theis, F.J. (2020). Generalizing RNA velocity to transient cell states through dynamical modeling. *Nat. Biotechnol.* 38, 1408–1414.
- Britz, O., Mattar, P., Nguyen, L., Langevin, L.M., Zimmer, C., Alam, S., Guillemot, F., and Schuurmans, C. (2006). A role for proneural genes in the maturation of cortical progenitor cells. *Cereb. Cortex* 16 (Suppl 1), i138–i151.
- Cabili, M.N., Trapnell, C., Goff, L., Koziol, M., Tazon-Vega, B., Regev, A., and Rinn, J.L. (2011). Integrative annotation of human large intergenic noncoding RNAs reveals global properties and specific subclasses. *Genes Dev.* 25, 1915–1927.
- Campbell, J.N., Macosko, E.Z., Fenselau, H., Pers, T.H., Lyubetskaya, A., Tenen, D., Goldman, M., Versteegen, A.M., Resch, J.M., McCarroll, S.A., et al. (2017). A molecular census of arcuate hypothalamus and median eminence cell types. *Nat. Neurosci.* 20, 484–496.
- Cao, J., Spielmann, M., Qiu, X., Huang, X., Ibrahim, D.M., Hill, A.J., Zhang, F., Mundlos, S., Christiansen, L., Steemers, F.J., et al. (2019). The single-cell transcriptional landscape of mammalian organogenesis. *Nature* 566, 496–502.
- Chen, X., Xu, H., Yuan, P., Fang, F., Huss, M., Vega, V.B., Wong, E., Orlov, Y.L., Zhang, W., Jiang, J., et al. (2008). Integration of external signaling pathways with the core transcriptional network in embryonic stem cells. *Cell* 133, 1106–1117.
- Chen, R., Wu, X., Jiang, L., and Zhang, Y. (2017). Single-cell RNA-seq reveals hypothalamic cell diversity. *Cell Rep.* 18, 3227–3241.
- Choi, H.M.T., Schwarzkopf, M., Fornace, M.E., Acharya, A., Artavanis, G., Stegmaier, J., Cunha, A., and Pierce, N.A. (2018). Third-generation *in situ* hybridization chain reaction: multiplexed, quantitative, sensitive, versatile, robust. *Development* 145, dev165753.
- Clark, D.D., Gorman, M.R., Hatori, M., Meadows, J.D., Panda, S., and Mellon, P.L. (2013). Aberrant development of the suprachiasmatic nucleus and circadian rhythms in mice lacking the homeodomain protein Six6. *J. Biol. Rhythms* 28, 15–25.
- Cooley, S.M., Hamilton, T., Deeds, E.J., and Ray, J.C.J. (2019). A novel metric reveals previously unrecognized distortion in dimensionality reduction of scRNA-Seq data. *bioRxiv*. <https://doi.org/10.1101/689851>.
- Fode, C., Ma, Q., Casarosa, S., Ang, S.L., Anderson, D.J., and Guillemot, F. (2000). A role for neural determination genes in specifying the dorsoventral identity of telencephalic neurons. *Genes Dev.* 14, 67–80.
- Fuentelba, L.C., Rompani, S.B., Parraguez, J.I., Obernier, K., Romero, R., Cepko, C.L., and Alvarez-Buylla, A. (2015). Embryonic origin of postnatal neural stem cells. *Cell* 161, 1644–1655.
- Gao, Y., and Sun, T. (2016). Molecular regulation of hypothalamic development and physiological functions. *Mol. Neurobiol.* 53, 4275–4285.
- Gao, P., Postiglione, M.P., Krieger, T.G., Hernandez, L., Wang, C., Han, Z., Streicher, C., Papusheva, E., Insolera, R., Chugh, K., et al. (2014). Deterministic progenitor behavior and unitary production of neurons in the neocortex. *Cell* 159, 775–788.
- Gomes, F.L., Zhang, G., Carbonell, F., Correa, J.A., Harris, W.A., Simons, B.D., and Cayouette, M. (2011). Reconstruction of rat retinal progenitor cell lineages

- in vitro reveals a surprising degree of stochasticity in cell fate decisions. *Development* 138, 227–235.
- Guillemot, F. (2005). Cellular and molecular control of neurogenesis in the mammalian telencephalon. *Curr. Opin. Cell Biol.* 17, 639–647.
- Gulati, G.S., Sikandar, S.S., Wesche, D.J., Manjunath, A., Bharadwaj, A., Berger, M.J., Ilagan, F., Kuo, A.H., Hsieh, R.W., Cai, S., et al. (2020). Single-cell transcriptional diversity is a hallmark of developmental potential. *Science* 367, 405–411.
- He, J., Zhang, G., Almeida, A.D., Cayouette, M., Simons, B.D., and Harris, W.A. (2012). How variable clones build an invariant retina. *Neuron* 75, 786–798.
- Hobert, O. (2004). Common logic of transcription factor and microRNA action. *Trends Biochem. Sci.* 29, 462–468.
- Hökfelt, T., Broberger, C., Xu, Z.Q., Sergeyev, V., Ubink, R., and Diez, M. (2000). Neuropeptides—an overview. *Neuropharmacology* 39, 1337–1356.
- Holguera, I., and Desplan, C. (2018). Neuronal specification in space and time. *Science* 362, 176–180.
- Ikeda, Y., Luo, X., Abbud, R., Nilson, J.H., and Parker, K.L. (1995). The nuclear receptor steroidogenic factor 1 is essential for the formation of the ventromedial hypothalamic nucleus. *Mol. Endocrinol.* 9, 478–486.
- Ishii, Y., and Bouret, S.G. (2012). Embryonic birthdate of hypothalamic leptin-activated neurons in mice. *Endocrinology* 153, 3657–3667.
- Johnson, M.B., Wang, P.P., Atabay, K.D., Murphy, E.A., Doan, R.N., Hecht, J.L., and Walsh, C.A. (2015). Single-cell analysis reveals transcriptional heterogeneity of neural progenitors in human cortex. *Nat. Neurosci.* 18, 637–646.
- Kee, N., Volakakis, N., Kirkeby, A., Dahl, L., Storvall, H., Nolbrant, S., Lahti, L., Björklund, A.K., Gillberg, L., Joodmardi, E., et al. (2017). Single-cell analysis reveals a close relationship between differentiating dopamine and subthalamic nucleus neuronal lineages. *Cell Stem Cell* 20, 29–40.
- Kohwi, M., and Doe, C.Q. (2013). Temporal fate specification and neural progenitor competence during development. *Nat. Rev. Neurosci.* 14, 823–838.
- Kokoeva, M.V., Yin, H., and Flieger, J.S. (2005). Neurogenesis in the hypothalamus of adult mice: potential role in energy balance. *Science* 310, 679–683.
- Kowalczyk, T., Pontious, A., Englund, C., Daza, R.A., Bedogni, F., Hodge, R., Attardo, A., Bell, C., Huttner, W.B., and Hevner, R.F. (2009). Intermediate neuronal progenitors (basal progenitors) produce pyramidal-projection neurons for all layers of cerebral cortex. *Cereb. Cortex* 19, 2439–2450.
- La Manno, G., Soldatov, R., Zeisel, A., Braun, E., Hochgerner, H., Petukhov, V., Lidschreiber, K., Kastriti, M.E., Lonnerberg, P., Furlan, A., et al. (2018). RNA velocity of single cells. *Nature* 560, 494–498.
- Lee, D.A., Bedont, J.L., Pak, T., Wang, H., Song, J., Miranda-Angulo, A., Takiar, V., Charubhumi, V., Balordi, F., Takebayashi, H., et al. (2012). Tanyocytes of the hypothalamic median eminence form a diet-responsive neurogenic niche. *Nat. Neurosci.* 15, 700–702.
- Leone, D.P., Srinivasan, K., Chen, B., Alcamo, E., and McConnell, S.K. (2008). The determination of projection neuron identity in the developing cerebral cortex. *Curr. Opin. Neurobiol.* 18, 28–35.
- Lo, L., Dormand, E., Greenwood, A., and Anderson, D.J. (2002). Comparison of the generic neuronal differentiation and neuron subtype specification functions of mammalian achaete-scute and atonal homologs in cultured neural progenitor cells. *Development* 129, 1553–1567.
- Loo, L., Simon, J.M., Xing, L., McCoy, E.S., Niehaus, J.K., Guo, J., Anton, E.S., and Zylka, M.J. (2019). Single-cell transcriptomic analysis of mouse neocortical development. *Nat. Commun.* 10, 134.
- Marín, O., and Müller, U. (2014). Lineage origins of GABAergic versus glutamatergic neurons in the neocortex. *Curr. Opin. Neurobiol.* 26, 132–141.
- Mayer, C., Hafemeister, C., Bandler, R.C., Machold, R., Batista Brito, R., Jaglin, X., Allaway, K., Butler, A., Fishell, G., and Satija, R. (2018). Developmental diversification of cortical inhibitory interneurons. *Nature* 555, 457–462.
- McConnell, S.K. (1991). The generation of neuronal diversity in the central nervous system. *Annu. Rev. Neurosci.* 14, 269–300.
- Mi, D., Li, Z., Lim, L., Li, M., Moissidis, M., Yang, Y., Gao, T., Hu, T.X., Pratt, T., Price, D.J., et al. (2018). Early emergence of cortical interneuron diversity in the mouse embryo. *Science* 360, 81–85.
- Moffitt, J.R., Bambah-Mukku, D., Eichhorn, S.W., Vaughn, E., Shekhar, K., Perez, J.D., Rubinstein, N.D., Hao, J., Regev, A., Dulac, C., and Zhuang, X. (2018). Molecular, spatial, and functional single-cell profiling of the hypothalamic preoptic region. *Science* 362, eaau5324.
- Morales-Delgado, N., Merchan, P., Bardet, S.M., Ferrán, J.L., Puelles, L., and Díaz, C. (2011). Topography of somatostatin gene expression relative to molecular progenitor domains during ontogeny of the mouse hypothalamus. *Front. Neuroanat.* 5, 10.
- Nowakowski, T.J., Bhaduri, A., Pollen, A.A., Alvarado, B., Mostajo-Radji, M.A., Di Lullo, E., Haeussler, M., Sandoval-Espinosa, C., Liu, S.J., Velmeshev, D., et al. (2017). Spatiotemporal gene expression trajectories reveal developmental hierarchies of the human cortex. *Science* 358, 1318–1323.
- Pak, T., Yoo, S., Miranda-Angulo, A.L., Wang, H., and Blackshaw, S. (2014). Rx-CreERT2 knock-in mice: a tool for selective and conditional gene deletion in progenitor cells and radial glia of the retina and hypothalamus. *PLoS ONE* 9, e90381.
- Parras, C.M., Schuurmans, C., Scardigli, R., Kim, J., Anderson, D.J., and Guillemot, F. (2002). Divergent functions of the proneural genes Mash1 and Ngn2 in the specification of neuronal subtype identity. *Genes Dev.* 16, 324–338.
- Patriarchi, T., Cho, J.R., Merten, K., Howe, M.W., Marley, A., Xiong, W.H., Folk, R.W., Broussard, G.J., Liang, R., Jang, M.J., et al. (2018). Ultrafast neuronal imaging of dopamine dynamics with designed genetically encoded sensors. *Science* 360, eaat4422.
- Petryniak, M.A., Potter, G.B., Rowitch, D.H., and Rubenstein, J.L. (2007). Dlx1 and Dlx2 control neuronal versus oligodendroglial cell fate acquisition in the developing forebrain. *Neuron* 55, 417–433.
- Pilz, G.A., Bottes, S., Betizeau, M., Jörg, D.J., Carta, S., Simons, B.D., Helmchen, F., and Jessberger, S. (2018). Live imaging of neurogenesis in the adult mouse hippocampus. *Science* 359, 658–662.
- Puelles, L., Martinez-de-la-Torre, M., Bardet, S., and Rubenstein, J.L.R. (2012). Hypothalamus. In *The Mouse Nervous System*, C. Watson, G. Paxinos, and L. Puelles, eds. (Academic Press), pp. 221–336.
- Qiu, X., Mao, Q., Tang, Y., Wang, L., Chawla, R., Pliner, H.A., and Trapnell, C. (2017). Reversed graph embedding resolves complex single-cell trajectories. *Nat. Methods* 14, 979–982.
- Quarta, C., Fisette, A., Xu, Y., Colldén, G., Legutko, B., Tseng, Y.T., Reim, A., Wierer, M., De Rosa, M.C., Klaus, V., et al. (2019). Functional identity of hypothalamic melanocortin neurons depends on Tbx3. *Nat. Metab.* 1, 222–235.
- Romanov, R.A., Alpár, A., Hökfelt, T., and Harkany, T. (2019). Unified Classification of Molecular, Network, and Endocrine Features of Hypothalamic Neurons. *Annu. Rev. Neurosci.* 42, 1–26.
- Romanov, R.A., Tretiakov, E.O., Kastriti, M.E., Zupancic, M., Häring, M., Korchynska, S., Popadin, K., Benevento, M., Rebernig, P., Lallemand, F., et al. (2020). Molecular design of hypothalamus development. *Nature* 582, 246–252.
- Saelens, W., Cannoodt, R., Todorov, H., and Saeys, Y. (2019). A comparison of single-cell trajectory inference methods. *Nat. Biotechnol.* 37, 547–554.
- Sato, T.K., Panda, S., Miraglia, L.J., Reyes, T.M., Rudic, R.D., McNamara, P., Naik, K.A., FitzGerald, G.A., Kay, S.A., and Hogenesch, J.B. (2004). A functional genomics strategy reveals Rora as a component of the mammalian circadian clock. *Neuron* 43, 527–537.
- Sharma, N., Flaherty, K., Lezgiyeva, K., Wagner, D.E., Klein, A.M., and Ginty, D.D. (2020). The emergence of transcriptional identity in somatosensory neurons. *Nature* 577, 392–398.
- Shirasaki, R., and Pfaff, S.L. (2002). Transcriptional codes and the control of neuronal identity. *Annu. Rev. Neurosci.* 25, 251–281.
- Sternson, S.M. (2013). Hypothalamic survival circuits: blueprints for purposive behaviors. *Neuron* 77, 810–824.

- Stuart, T., Butler, A., Hoffman, P., Hafemeister, C., Papalexi, E., Mauck, W.M., 3rd, Hao, Y., Stoeckius, M., Smibert, P., and Satija, R. (2019). Comprehensive Integration of Single-Cell Data. *Cell* 177, 1888–1902.e21.
- Suo, S., Zhu, Q., Saadatpour, A., Fei, L., Guo, G., and Yuan, G.C. (2018). Revealing the Critical Regulators of Cell Identity in the Mouse Cell Atlas. *Cell Rep.* 25, 1436–1445.e3.
- Telley, L., Agirman, G., Prados, J., Amberg, N., Fièvre, S., Oberst, P., Bartolini, G., Vitali, I., Cadilhac, C., Hippenmeyer, S., et al. (2019). Temporal patterning of apical progenitors and their daughter neurons in the developing neocortex. *Science* 364, eaav2522.
- Tirosh, I., Izar, B., Prakadan, S.M., Wadsworth, M.H., 2nd, Treacy, D., Trombetta, J.J., Rotem, A., Rodman, C., Lian, C., Murphy, G., et al. (2016). Dissecting the multicellular ecosystem of metastatic melanoma by single-cell RNA-seq. *Science* 352, 189–196.
- Tran, T.N., and Bader, G.D. (2020). Tempora: Cell trajectory inference using time-series single-cell RNA sequencing data. *PLoS Comput. Biol.* 16, e1008205.
- Trapnell, C., Cacchiarelli, D., Grimsby, J., Pokharel, P., Li, S., Morse, M., Lennon, N.J., Livak, K.J., Mikkelsen, T.S., and Rinn, J.L. (2014). The dynamics and regulators of cell fate decisions are revealed by pseudotemporal ordering of single cells. *Nat. Biotechnol.* 32, 381–386.
- Wang, F., Flanagan, J., Su, N., Wang, L.C., Bui, S., Nielson, A., Wu, X., Vo, H.T., Ma, X.J., and Luo, Y. (2012). RNAscope: a novel *in situ* RNA analysis platform for formalin-fixed, paraffin-embedded tissues. *J. Mol. Diagn.* 14, 22–29.
- Wen, S., Ma, D., Zhao, M., Xie, L., Wu, Q., Gou, L., Zhu, C., Fan, Y., Wang, H., and Yan, J. (2020). Spatiotemporal single-cell analysis of gene expression in the mouse suprachiasmatic nucleus. *Nat. Neurosci.* 23, 456–467.
- Wolf, F.A., Angerer, P., and Theis, F.J. (2018). SCANPY: large-scale single-cell gene expression data analysis. *Genome Biol.* 19, 15.
- Wolf, F.A., Hamey, F.K., Plass, M., Solana, J., Dahlin, J.S., Göttgens, B., Rajewsky, N., Simon, L., and Theis, F.J. (2019). PAGA: graph abstraction reconciles clustering with trajectory inference through a topology preserving map of single cells. *Genome Biol.* 20, 59.
- Wong, S.Z.H., Scott, E.P., Mu, W., Guo, X., Borgenheimer, E., Freeman, M., Ming, G.L., Wu, Q.F., Song, H., and Nakagawa, Y. (2018). *In vivo* clonal analysis reveals spatiotemporal regulation of thalamic nucleogenesis. *PLoS Biol.* 16, e2005211.
- Xiao, Y., Hill, M.C., Zhang, M., Martin, T.J., Morikawa, Y., Wang, S., Moise, A.R., Wythe, J.D., and Martin, J.F. (2018). Hippo Signaling Plays an Essential Role in Cell State Transitions during Cardiac Fibroblast Development. *Dev. Cell* 45, 153–169.e6.
- Xie, Y., and Dorsky, R.I. (2017). Development of the hypothalamus: conservation, modification and innovation. *Development* 144, 1588–1599.
- Xu, M., Wang, J., Guo, X., Li, T., Kuang, X., and Wu, Q.F. (2018). Illumination of neural development by *in vivo* clonal analysis. *Cell Regen. (Lond.)* 7, 33–39.
- Yu, G., Wang, L.G., Han, Y., and He, Q.Y. (2012). clusterProfiler: an R package for comparing biological themes among gene clusters. *OMICS* 16, 284–287.
- Zhong, S., Zhang, S., Fan, X., Wu, Q., Yan, L., Dong, J., Zhang, H., Li, L., Sun, L., Pan, N., et al. (2018). A single-cell RNA-seq survey of the developmental landscape of the human prefrontal cortex. *Nature* 555, 524–528.

STAR★METHODS

KEY RESOURCES TABLE

REAGENT or RESOURCE	SOURCE	IDENTIFIER
Antibodies		
Goat polyclonal anti-Sox2	R&D Systems	Cat#AF2018; RRID: AB_355110
Mouse monoclonal anti-GFAP	Merk-Millipore	Cat#MAB360; RRID: AB_11212597
Rat monoclonal anti-GFAP	Thermo Fisher Scientific	Cat#13-0300; RRID: AB_2532994
Mouse monoclonal anti- BLBP	Abcam	Cat#ab131137; RRID: AB_11157091
Rabbit monoclonal anti- Vimentin	Abcam	Cat#ab92547; RRID: AB_10562134
Rabbit polyclonal anti-RFP	Rockland	Cat#600-401-379; RRID: AB_2209751
Mouse monoclonal anti-Ascl1	BD Biosciences	Cat#556604; RRID: AB_396479
Rabbit polyclonal anti-Ascl1	Cosmo Bio	Cat#CAC-SK-T01-003; RRID: AB_10709354
Mouse monoclonal anti- Neurog2	R&D Systems	Cat#MAB3314; RRID: AB_2149520
Rabbit polyclonal anti-TH	Novusbio	Cat#NB300-109; RRID: AB_350437
Sheep polyclonal anti- Pitx2	R&D Systems	Cat#AF7388; RRID: AB_11128639
Rabbit polyclonal anti-Barhl1	Novusbio	Cat#NBP1-86513; RRID: AB_11034569
Chicken polyclonal anti-GFP	Aves Labs	Cat#GFP-1010; RRID: AB_2307313
Rat monoclonal anti- mCherry	Thermo Fisher Scientific	Cat#M11217; RRID: AB_2536611
Goat polyclonal anti- mCherry	Biorbyt	Cat#orb11618; RRID: AB_2687829
Rabbit polyclonal anti- Pomp	Phoenix Pharmaceuticals	Cat#H-029-30; RRID: AB_2307442
Goat anti-Agrp	Neuromics	Cat#GT15023; RRID: AB_2687600
Rabbit polyclonal anti-Sst	Phoenix Pharmaceuticals	Cat#H-060-03; RRID: AB_2687415
Rabbit polyclonal anti-Olig2	Engibody	Cat#AT0681; RRID: AB_2811222
Rabbit polyclonal anti-Otp	GeneTex	Cat#GTX119601; RRID: AB_11164017
Rabbit polyclonal anti-Islet1	Abcam	Cat#ab20670; RRID: AB_881306
Rabbit polyclonal anti-Nr5a1	TransGenic	Cat#KO611; RRID: AB_2861370
Goat polyclonal anti-Foxb1	Abcam	Cat#ab5274; RRID: AB_304806
Rabbit polyclonal anti-Tbr1	Abcam	Cat#ab31940; RRID: AB_2200219
Cy2 AffiniPure Donkey Anti-Mouse IgG (H+L)	Jackson ImmunoResearch Labs	Cat#715-225-150; RRID: AB_2340826
Cy2 AffiniPure Donkey Anti-Rabbit IgG (H+L)	Jackson ImmunoResearch Labs	Cat#711-225-152; RRID: AB_2340612
Cy2 AffiniPure Donkey Anti-Goat IgG (H+L)	Jackson ImmunoResearch Labs	Cat#705-225-147; RRID: AB_2307341
Cy2 AffiniPure Donkey Anti-Chicken IgY (IgG) (H+L)	Jackson ImmunoResearch Labs	Cat#703-225-155; RRID: AB_2340370
Cy2 AffiniPure Donkey Anti-Rat IgG (H+L)	Jackson ImmunoResearch Labs	Cat#712-225-150; RRID: AB_2340673
Cy3 AffiniPure Donkey Anti-Goat IgG (H+L)	Jackson ImmunoResearch Labs	Cat#705-165-003; RRID: AB_2340411
Cy3 AffiniPure Donkey Anti-Rat IgG (H+L)	Jackson ImmunoResearch Labs	Cat#712-007-003; RRID: AB_2340634
Cy3 AffiniPure Donkey Anti-Rabbit IgG (H+L)	Jackson ImmunoResearch Labs	Cat#711-165-152; RRID: AB_2307443
Cy3 AffiniPure Donkey Anti-Sheep IgG (H+L)	Jackson ImmunoResearch Labs	Cat#713-165-147; RRID: AB_2315778
Cy5 AffiniPure Donkey Anti-Rabbit IgG (H+L)	Jackson ImmunoResearch Labs	Cat#711-175-152; RRID: AB_2340607
Cy5 AffiniPure Donkey Anti-Mouse IgG (H+L)	Jackson ImmunoResearch Labs	Cat#715-007-003; RRID: AB_2307338
Cy5 AffiniPure Donkey Anti-Goat IgG (H+L)	Jackson ImmunoResearch Labs	Cat#705-175-147; RRID: AB_2340415
Cy5 AffiniPure Donkey Anti-Rat IgG (H+L)	Jackson ImmunoResearch Labs	Cat#712-175-150; RRID: AB_2340671

(Continued on next page)

Continued

REAGENT or RESOURCE	SOURCE	IDENTIFIER
Chemicals, peptides, and recombinant proteins		
Tamoxifen	Sigma-Aldrich	T5648
DAPI	Sigma-Aldrich	Cat#D9542
EdU	Ark Pharm	Cat#AK163060
Sulfo-Cy3 azide	Lumiprobe	Cat#C1330
Papain	Worthington	Cat#LK003178
DNaseI	Worthington	Cat#LK003172
Chondroitinase ABC	Sigma-Aldrich	Cat#C3667
Hyaluronidase	Rhawn	Cat#R006687
Glutamax	Life Technologies	Cat#35050061
D-(–)-2-Amino-5-phosphonopentanoic Acid	Sigma-Aldrich	Cat# 165304
Y27632 dihydrochloride	Sigma-Aldrich	Cat#T9531
B27 supplement	Thermo Fisher Scientific	Cat#17504044
Hibernate-E media	Life Technologies	Cat#A1247601
Tissue-Tek O.C.T. Compound	Sakura	Cat#4583
Critical commercial assays		
RNAscope® Multiplex Fluorescent Detection Reagents v2	Advanced Cell Diagnostics	Cat#323110
RNAscope® Target Retrieval Reagents	Advanced Cell Diagnostics	Cat#322000
RNAscope® Wash Buffer Reagents	Advanced Cell Diagnostics	Cat#310091
RNAscope® H2O2 and Protease Reagents	Advanced Cell Diagnostics	Cat#322381
TSA Plus Fluorescence kits	Perkin Elmer	Cat#NEL753001KT
Gel Bead Kit V3	10 x Genomics	Cat#1000075
Deposited data		
Supplementary Mendeley Figures	Mendeley Data	https://dx.doi.org/10.17632/f72pdw59zr.1
Raw data files for RNA Sequencing	NCBI GEO	GEO: GSE151060
Experimental models: organisms/strains		
Mouse: <i>Rax</i> ^{tm1.1(cre/ERT2)Sb1s/J}	The Jackson Laboratory	RRID: IMSR_JAX:025521
Mouse: <i>Gli1</i> ^{tm3(cre/ERT2)Alj/J}	The Jackson Laboratory	RRID: IMSR_JAX:007913
Mouse: <i>B6.Cg-Gt(ROSA)26Sor</i> ^{tm1(CAG-tdTomato)Hze/J}	The Jackson Laboratory	RRID: IMSR_JAX:007914
Mouse: <i>B6.Cg-Gt(ROSA)26Sor</i> ^{tm6.2(CAG-tdTomato)Hze/J}	The Jackson Laboratory	RRID: IMSR_JAX:032864
Mouse: <i>Igs2</i> ^{tm2(ACTB-tdTomato,-EGFP)Luo/J}	The Jackson Laboratory	RRID: IMSR_JAX:013751
Mouse: <i>Igs2</i> ^{tm1(ACTB-EGFP,-tdTomato)Luo/J}	The Jackson Laboratory	RRID: IMSR_JAX:013749
Mouse: Neurog2-FlpER ^{T2}	Songhai Shi's Laboratory	N/A
Mouse: C57BL/6J-Tg(Nkx2-1-cre)2Sand/J	The Jackson Laboratory	RRID: IMSR_JAX:008661
Mouse: <i>Ascl1</i> ^{tm1.1(Cre/ERT2)Jejo/J}	The Jackson Laboratory	RRID: IMSR_JAX:012882
Mouse: <i>Sst</i> ^{tm2.1(cre)Zjh/J}	The Jackson Laboratory	RRID: IMSR_JAX:013044
Mouse: <i>Tbx3</i> ^{Flox/Flox}	Frank et al., 2013	N/A
Oligonucleotides		
For hybridization chain reaction probe sequences, please see Table S7	This paper	N/A
Software and algorithms		
ZEN/ZEN2.3	Zeiss	N/A
Leica Application Suite X	Leica	N/A
ImageJ	National Institute of Health	https://imagej.net/Welcome ; RRID: SCR_003070

(Continued on next page)

Continued

REAGENT or RESOURCE	SOURCE	IDENTIFIER
GraphPad Prism 7	GraphPad Software	https://www.graphpad.com:443/ ; RRID: SCR_002798
Imaris v9.0.1	Bitplane	https://imaris.oxinst.com/packages/ ; RRID: SCR_007370
Reconstruct v1.1.0	J. C. Fiala	https://synapseweb.clm.utexas.edu/software-0/
Microsoft Excel	Microsoft	https://www.microsoft.com/en-gb/ ; RRID: SCR_016137
R v3.6.3	R Foundation	https://www.r-project.org/ ; RRID: SCR_001905
Python v3.7.8	Python Software Foundation	https://www.python.org/ ; RRID: SCR_008394
MATLAB v9.6.0	MathWorks	https://www.mathworks.com/products/matlab/ ; RRID: SCR_001622
Adobe Photoshop	Adobe	https://www.adobe.com/products/photoshop.html ; RRID: SCR_014199
Adobe Illustrator	Adobe	https://www.adobe.com/products/illustrator.html ; RRID: SCR_010279
Cell Ranger v3.0.2	10x Genomics	https://www.10xgenomics.com/ ; RRID: SCR_017344
Seurat v3	Stuart et al., 2019	https://satijalab.org/seurat/ ; RRID: SCR_016341
clusterProfiler	Yu et al., 2012	https://bioconductor.org/packages/release/bioc/html/clusterProfiler.html ; RRID: SCR_016884
Monocle 2	Trapnell et al., 2014	http://cole-trapnell-lab.github.io/monocle-release/docs/ ; RRID: SCR_016339
Monocle 3	Cao et al., 2019	https://cole-trapnell-lab.github.io/monocle3/ ; RRID: SCR_018685
velocyto	La Manno et al., 2018	http://velocyto.org/velocyto.py/citing/index.html ; RRID: SCR_018167
scVelo	Bergen et al., 2020	https://scvelo.readthedocs.io/ ; RRID: SCR_018168
CytoTRACE	Gulati et al., 2020	N/A
corrplot	Taiyun Wei	https://github.com/taiyun/corrplot
SCENIC	Aibar et al., 2017	https://github.com/aertslab/SCENIC ; RRID: SCR_017247
<hr/>		
Other		
RNAscope probe: Mouse <i>Slc17a6</i>	Advanced Cell Diagnostics	Cat#319171
RNAscope probe: Mouse <i>Slc32a1</i>	Advanced Cell Diagnostics	Cat#319191
RNAscope probe: Mouse <i>Hmx3</i>	Advanced Cell Diagnostics	Cat#518641-C2
HCRprobe	N/A	https://github.com/GradinaruLab/HCRprobe
Allen Developing Mouse Brain Atlas	N/A	http://developingmouse.brain-map.org/ ; RRID: SCR_002990
Lecia M205 fluorescence stereomicroscope	Leica	N/A
Leica SP8 confocal microscope	Leica	N/A
Zeiss LSM 710 confocal microscopy	Carl Zeiss	N/A
Leica CM3050 S Cryostat	Leica	N/A
BD FACSAria II flow cytometer	BD Bioscience	N/A
S1000TM Touch Thermal Cycler	Bio-Rad	N/A
SuperFrost Plus microscope slides	Thermo Fisher Scientific	Cat#12-550-15

RESOURCE AVAILABILITY**Lead contact**

Further information and requests for resources and reagents should be directed to and will be fulfilled by the Lead Contact, Qing-Feng Wu (wu_qingfeng@genetics.ac.cn).

Materials availability

All animals and unique/stable reagents generated in this study are available from the Lead Contact with a completed Materials Transfer Agreement.

Data and code availability

The accession number for the data reported in this paper is GEO: GSE151060. All software tools can be found online (see [Key resources table](#)). Complementing supplemental figures have been deposited to Mendeley Data and can be accessed using the following link: <https://dx.doi.org/10.17632/f72pdw59zr.1>.

EXPERIMENTAL MODEL AND SUBJECT DETAILS

Rax-CreER^{T2} (Stock No. 025521), *Gli1-CreER^{T2}* (Stock No. 007913), *Ai14* (Stock No. 007914), *Ai65F* (Stock No. 032864), *MADM-11^{TG}* (Stock No. 013751), and *MADM-11^{GT}* (Stock No. 013749) mouse strains were obtained from the Jackson Laboratory. *Neurog2-FlpER^{T2}*, *Nkx2.1-Cre* (Stock No. 008661), *Ascl1-CreER^{T2}* (Stock No. 012882), *Sst-IRES-Cre* (Stock No. 013044) and *Tbx3^{FloxFlox}* mouse lines were kindly provided by Dr. Songhai Shi, Dr. Zhen-gang Yang, Dr. Man Jiang, Dr. Peng Cao and Dr. Anne Moon's laboratory, respectively. MADM labeling technology relies on two reciprocally complementary chimeric marker genes (GT or TG) that have been knocked into the same locus on homologous chromosomes. Tamoxifen-induced nuclear translocation of Cre recombinase mediates the interchromosomal recombination in the G2 phase of cell cycle, which recovers the functional marker genes. While G2-X segregation of chromatids generates a pair of differentially labeled green and red cells, G2-Z segregation yields a double-labeled yellow cell and an unlabeled cell. Recombination in G1 phase or postmitotic cells (G0) generates a dual-labeled cell. Animals were maintained on a 12h light-dark cycle with libitum access to food and water. All animal procedures used in this study were performed according to protocols approved by the Institutional Animal Care and Use Committee at Institute of Genetics and Developmental Biology, Chinese Academy of Sciences.

METHOD DETAILS**Tamoxifen Induction**

To trace the hypothalamic cell lineages, we bred *Rax-CreER^{T2}* and *Ascl1-CreER^{T2}* mice with *Ai14* reporter mice, crossed *Neurog2-FlpER^{T2}* mice with *Ai65F* reporter mice, checked the vaginal plug to determine the time of pregnancy and intraperitoneally injected a single dose of tamoxifen (132 mg/kg body weight) into timed pregnant females to label *Rax⁺* hypothalamic neuroepithelium at E9 or *Ascl1⁺* HIPC1 and *Neurog2⁺* HIPC2 at E11.5. TdTomato-labeled embryos were obtained by cesarean section and perfused intracardially with cold 4% paraformaldehyde (PFA) in phosphate-buffered saline (PBS). To collect postnatal brains, we recovered live embryos at E18-E19 by cesarean section, cared the pups with foster female animals and collected the postnatal mice for further analyses.

EdU Pulse-Chase Assay

To investigate the birthdate of postnatal tanycytes, we performed pulse-chase assay by intraperitoneally apply a single dose of EdU (200 mg/kg body weight) into timed pregnant female animals at E11, E13, E14, E15 and E18 to label dividing cells. The pups were anesthetized on ice, intracardially perfused with 4% PFA and dissected to collect the brain tissues at P7 for analyzing the label-retaining cells. For cell quantification, the number of EdU⁺Sox2⁺GFAP⁺ cells was divided by the total counts of Sox2⁺GFAP⁺ cells lining the third ventricle to index the ratio of label-retained cells.

Single-Cell Isolation

We isolated single cells from *Rax-CreER^{T2}::Ai14* mice as previously described with minor modifications ([Moffitt et al., 2018](#)). Briefly, the brain tissues were harvested at E11, E14, P0 and P7, followed by the microdissection of hypothalamic tissues under fluorescence stereomicroscope (Lecia M205, Leica Microsystems, Germany). The microdissected tissues were transferred to a 24-well cell culture plate and treated with papain digestion buffer comprising 10 U/mL Papain (Worthington, LK003178), 200 U/mL DNaseI (Worthington, LK003172), 0.5 U/mL chondroitinase ABC (Sigma, C3667), 0.07% hyaluronidase (Rhawn, R006687), 1 × Glutamax (Life Technologies, 35050061), 0.05 mM D-(–)-2-Amino-5-phosphonopentanoic Acid(Sigma-Aldrich, 165304), 0.01 mM Y27632 dihydrochloride (Sigma, T9531), and 0.2 × B27 supplement (Thermo Fisher Scientific, 17504044) in Hibernate-E media (Life Technologies, A1247601). After digesting 15-30 min (embryonic brains) or 1-1.5 hr (postnatal brains) at 37°C, the papain digestion buffer was changed into Hibernate-E buffer containing 1 × Glutamax, 0.05 mM APV, 0.2 × B27, 0.01 mM Y27632 dihydrochloride and 1% fetal bovine serum (FBS). Then tissues were gently triturated through Pasteur pipettes with finely-polished tips of 600-, 300- and 200-µm

diameters and washed once with Hibernate-E buffer to generate single-cell suspension. Subsequently, the dissociated hypothalamic cells were stained with DAPI (0.2 µg/mL) to identify dead cells and subjected to fluorescence-activated cell sorting (FACS; BD FACSAria II flow cytometer, BD Bioscience, U.S.A.) for isolating tdTomato-positive live cells.

Single-Cell RNA Library Preparation and Sequencing

Single-cell RNA-seq libraries were constructed according to the instructions provided by 10 × Genomics accompanying single cell 3' Library and Gel Bead Kit V3 (10 × Genomics, 1000075). Cell suspensions (300-600 living cells per microliter determined by Count Star) were loaded on a Chromium Single Cell Controller (10 × Genomics) to generate single-cell gel beads in the emulsion (GEM). Captured cells were lysed to release mRNA which were subsequently barcoded through reverse transcribing individual GEMs. Using a S1000TM Touch Thermal Cycler (Bio-Rad, U.S.A.) to reverse transcribe, the GEMs were programmed at 53°C for 45 min, followed by 85°C for 5 min and hold at 4°C. The cDNA library was then generated, amplified and assessed for quality control using the Agilent 4200. The single-cell RNA sequencing was further performed on the Illumina Novaseq6000 sequencer.

EdU Staining and Immunohistochemistry

The animals were anesthetized by hypothermia and then transcardially perfused with saline followed by 4% PFA in PBS. Mouse brains were immediately dissected, post-fixed for 4-6 hr in 4% PFA at 4°C, and subsequently cryo-protected in 20% sucrose in PBS for 12 hr followed by 30% sucrose for 24 hr. Tissue blocks were prepared by embedding in Tissue-Tek O.C.T. Compound (Sakura 4583). The brain sections (20-40 µm in thickness) were prepared using a cryostat microtome (Leica, CM3050S), dried for 30 min at room temperature in the dark and stored in -20°C freezer. For immunostaining, the tissue sections were washed with 1 × TBS (pH = 7.4, containing 3 mM KCl, 25 mM Trizma base and 137 mM NaCl) and pre-blocked with 1 × TBS++ (TBS containing 5% donkey serum and 0.3% Triton X-100) for 1 hr at room temperature, followed by incubation with primary antibodies diluted in TBS++ overnight at 4°C. The primary antibodies used in this study included goat anti-Sox2 (R&D; AF2018; 1:250), mouse anti-GFAP (Merk-millipore; MAB360 ; 1:500), rat anti-GFAP (Thermofisher scientific; 13-0300; 1:1000), mouse anti-BLBP (Abcam; ab131137; 1:250), rabbit anti-Vimentin (Abcam; ab92547; 1:250), rabbit anti-RFP (Rockland; 600-401-379; 1:1000), mouse anti-Ascl1 (BD; 556604; 1:250), rabbit anti-Ascl1 (Cosmo Bio; CAC-SK-T01-003; 1:400), mouse anti-Neurog2 (R&D; MAB3314; 1:200), rabbit anti-TH (Novusbio; NB300-109; 1:500), sheep anti-Pitx2 (R&D; AF7388; 1:500), rabbit anti-Barhl1 (Novusbio; NBP1-86513; 1:500), chicken anti-GFP (Aves Labs; 1010; 1:500), rat anti-mCherry (Thermo Fisher Scientific; M11217; 1:500), goat anti-mCherry (Biorbyt; orb11618; 1:500), rabbit anti-Pomc (Phoenix pharmaceuticals; H-029-30; 1:200), goat anti-Agrp (Neuromics; GT15023; 1:500), rabbit anti-Sst (Phoenix pharmaceuticals; H-060-03; 1:500), rabbit anti-Olig2 (Engibody; AT0681; 1:200), rabbit anti-Otp (GeneTex; GTX119601; 1:200), rabbit anti-Islet1 (Abcam; ab20670; 1:200), rabbit anti-Nr5a1 (TransGenic; KO611; 1:200), goat anti-Foxb1 (Abcam; ab5274; 1:200) and rabbit anti-Tbr1 (Abcam; ab31940; 1:200). After primary antibody incubation, the brain sections were washed for 3 times with 1 × TBS and incubated with following secondary antibodies for 2 hr at room temperature: anti-mouse Cy2, anti-rabbit Cy3 and anti-rabbit Cy5 (Donkey; Jackson ImmunoResearch; 1:500).

For EdU labeling, the tissue sections were permeabilized with 0.5% Triton X-100 for 30 min and detected with detection solution containing 5 µM Sulfo-Cy3 azide (Lumiprobe, #C1330), 0.1 M Tris-HCl (pH = 7.5), 4 mM copper sulfate and 100 mM sodium ascorbate for 30 min. After staining, sections were coverslipped with mounting medium, air-dried overnight and maintained at 4°C in the dark for further imaging. The brain sections were imaged using Leica SP8 equipped with four lasers (405, 488, 568 and 647 nm).

Single-molecule Fluorescent in Situ Hybridization (smFISH)

To prepare tissue sections for smFISH, mouse brains were dissected, immersed in 4% PFA for 4-6 hr and then dehydrated with 20%-30% DEPC-treated sucrose for 24 hr. Subsequently, the tissues were rapidly frozen using dry ice, embedded in O.C.T. compound, cryosectioned at a thickness of 30 µm and mounted onto SuperFrost Plus microscope slides. The probes targeting against *Slc17a6* (Advanced Cell Diagnostics, #319171), *Slc32a1* (Advanced Cell Diagnostics, #319191) and *Hmx3* (Advanced Cell Diagnostics, #518641-C2) were designed and validated by Advanced Cell Diagnostics. RNAscope v2 Assay (Advanced Cell Diagnostics, #323110) was used for all smFISH experiments according to the manufacturer's protocol (Wang et al., 2012). Briefly, the brain sections were dried at 55°C for 2 hr, rinsed with 1 × PBS, treated with 3% hydrogen peroxide in methanol and subjected to antigen retrieval. Subsequently, the tissue sections were dehydrated with 100% ethanol and incubated with mRNA probes for 2 hr at 40°C. The specific signals were then amplified with multiplexed amplification buffer and detected with TSA Plus Fluorescence kits (Perkin Elmer, #NEL753001KT).

To detect the mRNA expression level of *Gal*, *Ghrh*, *Irx5*, *Lmx1a*, *Sst*, *Agrp*, *Pomc*, *Sox14*, *Dlx1*, *Fezf1*, *Cbln1*, *Tbx3* and *Tbx19*, we used hybridization chain reaction (HCR) approach (Choi et al., 2018). A software (available at <https://github.com/GradiaruLab/HCRprobe>) was used to design HCR probes for targeting coding sequence (CDS) and 3'UTR region of interest gene genes (Patriarchi et al., 2018). The sequences of all HCR probes are included in Table S6 and all of them were synthesized by Sangon Biotech, China. The brain sections were permeabilized in 70% ethanol for 16 hr at 4°C, followed by 0.5% Triton X-100 in 1 × PBS at 37°C for 1 hr, and treated with 10 µg/mL Protease K to improve mRNA accessibility. After two washes with 1 × PBS at room temperature, sections were pre-hybridized in 30% probe hybridization buffer for 1 hr at 37°C and then incubated in 30% probe hybridization buffer containing HCR probes (10 µM for each) at 37°C for 3 hr. After mRNA hybridization, the washing and amplification steps were performed as previously described (Choi et al., 2018). Immunofluorescence staining with antibodies against TH was further conducted on HCR-labeled sections.

Cross-Reference of Allen Mouse Brain Atlas

In situ images of mouse brains were resourced from Allen Developing Mouse Brain Atlas (<http://developingmouse.brain-map.org>). To map the spatial distribution of HIPC subtypes, we marked the peduncular and terminal regions along longitudinal axis, as well as preoptic, anterior, tuberal and mammillary zones along sagittal axis on the E13.5 reference sections. To identify the nucleus distribution of diverse neuronal subtypes, we referred the prenatal atlas and marked diverse hypothalamic nuclei on the E18.5 and P4 reference sections.

Pre-Processing of Sequencing Data

Read pre-processing was performed using the 10 × Genomics workflow. Briefly, the Cellranger's pipeline (version 3.0.2) was used for demultiplexing raw sequencing data, barcode assignment and quantification of unique molecular identifiers (UMIs). Using a pre-built annotation package, we mapped the reads to the mouse reference genome (GRCm38/mm10, release 93) to generate gene expression matrices. The matrix files arising from different batches of experiments were subsequently analyzed using Seurat v3 software ([Stuart et al., 2019](#)).

Quality Control and Data Integration

For quality control, we set the threshold and removed cells with more than 5% of reads mapping to mitochondrial genes (considered to be low-quality cells that exhibit extensive mitochondrial contamination), fewer than 2,000 genes (considered to be low-quality cells or empty droplets), more than 8,000 genes or 50,000 UMIs (considered likely to be cell doublets or multiplets), leaving 43,670 cells for further integrated analysis.

We integrated multiple datasets covering hypothalamic cells across four different time points using the standard integration workflow built in Seurat v3 software according to the tutorial at <http://satijalab.org/seurat/archive/v3.1/integration.html>. In brief, SCTransform normalization was implemented separately for each dataset, 2,000 variable feature genes were selected and the 'anchors' identified by 'FindIntegrationAnchors' function were used to integrate data.

Cell-Cycle Analysis

Variations in cell cycle stages, particularly among mitotic cells transitioning between S and G2/M phases, can lead to a substantial mask of authentic biological signals and thereby alter the cell clustering. Given that neural progenitor cells in the developing brain are mitotically active, we regressed out cell cycle variation to mitigate its adverse effect for clustering RGCs and IPCs by rescaling the score of 43 S-phase and 54 G2/M-phase genes as described previously ([Tirosh et al., 2016](#)). Briefly, we assigned cell cycle score for each cell using supervised analysis of the phase-specific genes, calculated the difference between G1/S and G2/M phase scores and subtracted the source of heterogeneity from our datasets to remove cell cycle effect.

Dimensionality Reduction and Clustering

With integrated expression values in hand, we detected the highly variable genes, performed principle component analysis (PCA) and selected the top 40 significant principle components (PCs) to perform Uniform Manifold Approximation and Projection (UMAP) analysis. Using UMAP algorithm, we reduced variation to two dimensions by 'RunUMAP' function and carried out unsupervised clustering of cells by constructing a shared nearest neighbor (SNN) graph according to K-nearest neighbors (K = 20) and then determining the number of clusters with a modularity function optimizer. The clusters were further compared pairwise to identify cell type-specific genes and the cell identities were assigned by cross-referencing their marker genes with known neural subtype markers. A small subpopulation of cells that ambiguously expressed multiple marker genes for different cell types was found to capture low level of UMIs and defined as low-quality cells or multiplets that escaped the first quality-control step and thereby excluded from further analyses. A final dataset of 43,261 individual cells with 28,868 genes was preserved to map the landscape of hypothalamus development and roughly classified into radial glial cells (RGCs), intermediate progenitor cells (IPCs), excitatory glutamatergic neurons, inhibitory GABAergic neurons, astrocytes, oligodendrocyte progenitor cells (OPCs), oligodendrocytes and ependymal cells. For sub-clustering, RGCs, IPCs and neurons were separately subsetted and reclustered with an optimal resolution based on the number of cells according to the Seurat guidelines. A dendrogram showing the relatedness of cell subclusters was generated for 29 neuronal subtypes based on a distance matrix constructed in PCA space (BuildClusterTree function).

Differential Gene Expression Analysis

To identify genes differentially expressed in cells of diverse types or at different developmental stages, we compared cell groups pairwise and identified differentially expressed genes using 'FindAllMarkers' function with Wilcoxon rank-sum test, which returned logarithmic fold-changes of the average gene expression among groups and adjusted *p* values for each tested gene based on Bonferroni correction. The top-ranking differentially expressed gene sets were chosen for further gene ontology (GO) enrichment analysis with clusterProfiler software ([Yu et al., 2012](#)). Functional enrichment of target gene sets in GO biological processes or cellular components was determined with hypergeometric test, setting *p* value threshold of 0.01 for statistical significance. Heatmaps of the differentially expressed genes was generated by ggplot2 package built with Seurat software.

Monocle Pseudotemporal Analysis

We performed pseudotemporal analysis using Monocle software to infer the developmental trajectory of hypothalamic cell lineage. The Monocle 3 pipeline (Cao et al., 2019) was applied to reconstruct the single-cell trajectories of subsetted hypothalamic cells covering neural progenitors and postmitotic neurons, given its optimized designing for large datasets and powerful ability to learn very complex, potentially disjoint trajectories. Briefly, we normalized the expression value by logarithmic transformation and assigned UMAP coordinates from the integrated Seurat object to ‘cell_data_set’ (CDS) object produced by Monocle 3 for trajectory inference. To abolish the effect of cluster size on the robustness of trajectory inference, we randomly subset a maximum of 2000 cells from each cluster of neural cells.

To simply reconstruct individual trajectories for neuronal and glial lineage, we subsetted neurons or glial cells to integrate with their progenitor cells and performed trajectory analysis using Monocle 2 (Qiu et al., 2017; Trapnell et al., 2014). To order the genes along pseudotime, we imported 2,000 variable features identified by Seurat, filtered out genes detected within lower than 5% of cells, applied ‘DDRTree’ to reduce dimensions and plotted the minimum spanning tree of cells. We then clustered genes by their pseudotemporal expression pattern and generated the heatmaps to visualize the transcriptional programs that co-vary across pseudotime. The trends of pseudotemporal gene expression for each transcriptional program were analyzed as previously reported (Xiao et al., 2018).

While Monocle 2 typically uses DDRTree algorithm to implement dimensional reduction and orders the cells by reverse graph embedding (Qiu et al., 2017), Monocle 3 does dimensional reduction with UMAP to construct an initial trajectory and refines it with learning principal graph (Cao et al., 2019). Although Monocle 3 has been designed to span most of cell types and learn very complex, potentially disjoint trajectories for large datasets, it has recently been reported to introduce spurious connections that are unlikely to occur biologically (Tran and Bader, 2020). Moreover, UMAP-based dimensional reduction may sometimes introduce distortion into the data and errors in the pseudotemporal ordering of cells (Cooley et al., 2019). Given that Monocle 3 is still under construction for better performance and Monocle 2 has recently passed a benchmark test (Saelens et al., 2019) to provide us simple, clear trajectory, we determined to perform a simultaneous analysis using Monocle 3 and Monocle 2 for different purposes.

Gene Expression Signature Scoring

Individual neuronal subtypes were scored for HIPC signature programs to infer the transcriptional connection between HIPC and neuronal subtypes. Briefly, the signature programs of HIPC subtypes were derived from the top-ranking variable genes identified by the ‘FindAllMarkers’ function with an ‘min.pct’ of 0.25 and ‘logfc.threshold’ of 0.25. We then scored individual neuronal subtypes for their enrichment of HIPC gene signatures using the function ‘AddModuleScore’ in Seurat.

RNA Velocity Analysis

RNA velocity approach can estimate the cell state by distinguishing between unspliced and spliced mRNAs in single-cell dataset, predict the future state of individual cells and infer their developmental trajectory (La Manno et al., 2018). Recently, scVelo (<https://scvelo.readthedocs.io/>) has been released to solve the full transcriptional dynamics of splicing kinetics through dynamical modeling and enhance the power of RNA velocity (Bergen et al., 2020). To infer the developmental trajectory, we first processed the BAM files outputted by Cell Ranger and generated a loom file containing spliced and unspliced transcript counts by applying velocyto command line tool (<http://velocyto.org/velocyto.py/citing/index.html>), which would be used as input to scVelo. After filtering out low quality/dying cells as aforementioned, we applied scVelo to normalize the dataset using default parameters, performed PCA on the spliced matrix using 30 principal components and produced KNN neighbor graph with k = 30. The RNA velocities were computed using the scvelo.tl.velocity() function based on stochastic model, the velocity graph was constructed based on the velocity vector with scvelo.tl.velocity_graph and velocities were ultimately projected as gridlines into UMAP embedding.

CytoTRACE Analysis

We leveraged CytoTRACE (cellular trajectory reconstruction analysis using gene counts and expression) approach, a recently developed computational method for predicting the direction of differentiation from scRNA-seq data across multiple developmental stages (Gulati et al., 2020), to recover the differentiation and maturation state of neurons in our dataset. The multiple single-cell datasets covering neurons and their immediate progenitors were re-integrated using ‘iCytoTRACE’ function and used to quantify the number of expressed genes as a simple, yet robust indicator of developmental potential. We further visualized the maturation state of neurons on the UMAP embeddings generated previously in Seurat.

Partition-based Graph Abstraction (PAGA) Analysis

To validate the lineage capacity of cycling RGCs, we applied PAGA, a built-in package in Scanpy, for inferring the developmental trajectory of RGCs (Wolf et al., 2018, 2019). Briefly, we used cluster identities from the Louvain algorithm (clusters annotated in Figure 2A) to define the partitions of the graph of neighborhood relations among data points. Graph abstraction was computed using the ‘tl.agp’ function implemented in the Python package Scanpy, and edges were drawn using the adjacency confidence matrix.

TF and Neuropeptide Modular Analysis

We first assessed the expression of 4,482 TFs and 100 peptides in diverse neuronal subtypes and identified 191 TFs and 34 neuropeptides with subtype-specific expression pattern. To determine the TF and peptide modules that define potential gene regulatory

network and neuronal subtype identities at the cluster level, we calculated the Pearson's correlation coefficients of subtype-specific TFs and neuropeptides/monoamine based on their averaged gene expression level in 29 neuronal subtypes. The correlation matrices were then imported to corplot R package (<https://github.com/taiyun/corplot>) for a graphical display.

Regulon Analyses for Neuronal Subtypes and Nuclei

Regulon scores for individual cells were computed using the SCENIC (single-cell regulatory network inference and clustering) pipeline (Aibar et al., 2017). A log-normalized expression matrix of neuronal cells was used as an input into the pySCENIC workflow (<https://pyscenic.readthedocs.io/en/latest/index.html>) with default settings to infer regulons (master TFs and their target genes). First, the potential TF targets were inferred based on our gene expression dataset using the 'grnboost2' function. Second, we identified a list of enriched TF-binding motifs and the corresponding target genes for all gene co-expression modules, and then uncovered the regulons based on the database containing motifs with genome-wide rankings. Third, the activity of each regulon across the cells was scored using the area under the recovery curve (AUC) threshold of genes that define this regulon. Lastly, average regulon activity for 313 identified regulons in 29 neuronal subtypes was computed and visualized as heatmap, which showed groups of regulons that tend to be active in each neuronal subtype. To quantify the cell-type specificity of a regulon, we converted regulon activity scores (RAS) to regulon specificity scores (RSS) based on the Jensen-Shannon Divergence (JSD) as previously described (Cabili et al., 2011; Suo et al., 2018), followed by the ranking of 313 regulons based on their RSS scores for each neuronal subtype. To gain insight into the gene regulatory networks potentially involved in nucleus specification, we pooled multiple neuronal clusters with the same nuclear distribution, inferred the average regulon activity for each identified hypothalamic nucleus and generated a heatmap to visualize the activity of regulons.

Clonal Analysis and Quantification

To label progenitor cells at a clonal level, we crossed *Rax-CreER^{T2}::MADM-11^{GT/GT}* or *Gli1-CreER^{T2}::MADM-11^{GT/GT}* male mice with *MADM-11^{TG/TG}* female mice, applied an optimized, single dose of tamoxifen (132mg/kg body weight) into pregnant *Rax-CreER^{T2}::MADM-11* mice at E10 and sacrificed the animals for brain collection at P0, P7 and P30. The brains were then serially sectioned at a thickness of 30 µm, immunostained with antibodies against GFP and tdTomato (or mCherry) to identify positive clones and imaged by Leica SP8 confocal microscope. For 3D reconstruction, optical stacks of images were serially aligned along the rostro-caudal axis using Reconstruct 1.1.0 (J.C. Fiala, NIH), followed by importing into Imaris (Bitplane) for further analysis. In the reconstructed brains, we created 'surfaces' by outlining the brain contour, 'spots' for each genetically-labeled cells, and 'filaments' for RGC radial process as previously described (Wong et al., 2018). The number of cells per clone was quantified to analyze the proliferative potential of labeled RGCs, and Graphpad Prism, Microsoft Excel, and R software were used for quantitative analysis. To quantify the clonal composition, we used Olig2 as oligodendrocyte lineage marker and GFAP as astrocyte marker to stain bushy cells without neuronal morphology. To assess the clonal organization, we measured the tangential and radial migration distance of progeny cells from RGCs by exporting from Imaris the digitized, discrete 3D position of individual cells ('spots') and radial processes ('filaments') and automatically computed the minimum distances to the nearest radial process in MATLAB. The minimum distance between each progeny cells and the radial process reflects the range of tangential migration, while the minimum distance along the radial process between each progeny cells and RGC implicates the range of radial migration.

To analyze the neuronal subtypes in arcuate clones, we consecutively sectioned the *Rax-CreER^{T2}::MADM-11* brains and split into three sets of glass slides. Each set of brain sections were stained with antibodies against GFP, mCherry and peptidergic neuronal markers. The putative neuronal subtype markers in arcuate nucleus (ARC), including AgRP, SST, POMC and TH, were used to evaluate the neuronal subtype identity.

QUANTIFICATION AND STATISTICAL ANALYSIS

General Statistical Analysis

All of the statistical details of experiments can be found in the figure legends and text. Graphpad Prism, Microsoft Excel, Python and R software were used for statistical analysis. All data collection and analysis were blinded in this study. In all cases, data are presented as mean ± standard error of the mean (SEM). Quantifications were statistically analyzed using either two-tailed unpaired Student's t test or one-way ANOVA. Statistical significance was indicated as follows: * p < 0.05; ** p < 0.01; *** p < 0.001. All experiments were independently repeated for at least three times.

Nearest Neighbor Distance Analysis

The distribution of nearest neighbor distance (NND) of labeled tdTomato+ cells, automatically scaled by ImageJ, reflects the spatial point pattern of the dataset, as previously described (Gao et al., 2014). In this analysis, we induced genetic labeling using *Rax-CreER^{T2}::Ai14* mice, collected the E10 brains at 1 day post tamoxifen injection, took the images of Rax-derived cells, measured the NND among thousands of labeled cells within the hypothalamic primordium and then performed density analysis.